Miguel Yerón Rojas Sánchez

Characterization of rectangular waveguides with metamaterials

Title project report for the degree of Electronic Civil Engineer

School of Electrical Engineering
Faculty of Engineering

Valparaiso, March 1st, 2019

Characterization of rectangular waveguides with metamaterials

Miguel Yerón Rojas Sánchez

Final Report to apply for the title of Electronic Civil Engineer,

approved by the commission of the

School of Electrical Engineering of the

Pontificia Universidad Católica de Valparaíso

conformed by

Mr. Francisco Pizarro Torres

First reviewer

Mrs. Nathalie Raveu

Second reviewer

Mr. Sebastián Fingerhuth Massmann

Academic secretary

Valparaíso, March 1st, 2019

Resumen

Se explican las razones de los metamateriales en la industria aeroespacial y el rápido interés que ha generado en este campo debido a sus propiedades únicas. En la sección 1, se introduce en el tema de los metamateriales y sus diferentes clasificaciones en función de los parámetros constitutivos de los materiales, que es la permitividad y la permeabilidad. La definición de lo que es un metamaterial se explica para luego definir algunos conceptos importantes que implicarán el desarrollo de este trabajo; Se aborda el tema de las superficies de alta impedancia, sus modelos analíticos, sus modelos numéricos y cómo son útiles para fabricar guías de ondas con paredes anisotrópicas. Más adelante, se detallan las Superficies Selectivas de Frecuencia, se muestran los diferentes patrones utilizados para obtener propiedades electromagnéticas especiales en función de la superficie diseñada.

La sección 2 se compone de un recordatorio sobre las guías de onda rectangulares, se desarrollan las ecuaciones que gobiernan en los medios guiados convencionales y luego se estudia la definición de la impedancia de superficie junto con las ecuaciones que la involucran.

La sección 3 presenta la caracterización modal de guías de onda rectangulares cargadas con diferentes impedancias de superficie anisotrópica como condicion de contorno en sus paredes verticales. Los diagramas de dispersión para estas guías de onda se calculan utilizando diferentes condiciones de contorno para las superficies de las paredes de impedancia anisotrópica, y luego se validan comparando los resultados calculados con los obtenidos con el software comercial ANSYS HFSS. Los resultados muestran propiedades interesantes de estas guías de onda cargadas con estas características de impedancia, como el desplazamiento de la frecuencia de corte en función del valor de una de las impedancias transversales, mientras que las otras impedancias son fijas, lo que permite, por ejemplo, reducir la sección transversal de una guía de onda WR770 un 87.16% e incrementar su ancho de banda en un 11.2% cuando se usa una impedancia $Z_{t1} = 2.5\, j\, Z_0$ por ejemplo.

La sección 4 muestra los diferentes diseños utilizados para obtener las impedancias que cumplen con los requisitos de ancho de banda y frecuencia de operación con respecto a las guías de onda convencionales analizadas en la sección 3

Se adjunta en el apéndice 1 el desarrollo detallado de las ecuaciones presentadas en la sección 3, y en el apéndice 2 se muestran los pasos utilizados en el software Ansys HFSS para simular una celda unitaria utilizando el puerto Floquet. Finalmente, el apéndice 3 contiene los gráficos de dispersión para los diferentes casos analizados en la sección 4.

Palabras claves: Teoría Modal Expandida, TEM, Diagrama de dispersion, Superficie de Alta Impedancia, SAI, Superficie anisotropica.

Abstract

The reasons for the metamaterials in the aerospace industry and the rapid interest it has generated in this field due to their unique properties are explained. In section 1, is introduced in the topic of metamaterials and their different classifications depending on the constitutive parameters of the materials, which is the permittivity and permeability. The definition of what it is a metamaterial is explained to then define some important concepts that will involve the development of this work; It is explained what are the High Impedance Surfaces, their analytical models, their numerical models and how they are useful to manufacture waveguides with anisotropic walls. Later, Frequency Selective Surfaces are explained, it is shown the different patterns used to obtain special electromagnetic properties depending of the surface designed.

Section 2 is composed of a reminder about rectangular waveguides, the equations that govern in conventional guided media are developed and then an explanation about the definition of surface impedance together with the equations that involve it.

Section 3 presents the modal characterization of rectangular waveguides loaded with different anisotropic surface impedance boundaries on their vertical walls. Dispersion diagrams for these waveguides are computed using various different boundary conditions for the anisotropic impedance walls surfaces, and then validated comparing the computed results with the ones obtained with the commercial software ANSYS HFSS. The results shows interesting properties of these waveguides loaded with this impedance characteristics, such as displacement of the cutoff frequency depending on the value of one of the transversal impedances meanwhile the other impedances are fix, which allows, for example, to reduce the cross section of a waveguide WR770 by 87.16% and increase its bandwidth by 11.2% when using an impedance $Z_{t1} = 2.5\,j\,Z_0$.

Section 4 shows the different designs used to obtain the impedances that meet the requirements of bandwidth and frequency of operation with respect to conventional waveguides analyzed in section 3

Attached in appendix 1 is the development of the equations presented in section 3, and in appendix 2 the steps taken in the Ansys HFSS software to simulate a unit cell using Floquet port is shown. Finally, appendix 3 contains the dispersion plots for the different cases tested in section 4.

Key words: Modal Expansion Theory, MET, Dispersion plot, High Impedance Surfaces, HIS, Anisotropic surface

Contents

Introduction

Wave propagation in guided topologies has been a subject of several studies over the whole microwave technologies development era [1], [2]. The results obtained of these studies led to many applications in terms of new software that can analyse and model a whole family of microwave topologies including filters, antennas, transducers and other structures [3]–[6] that before were difficult to achieve, and leading to the analysis of other complex structures, such as metamaterials [7]. These materials have electromagnetic properties that are not available in natural materials. For example, with metamaterials it is possible to obtain a relative permittivity and/or relative permeability with values lower than one, or even negative [8]. It is possible to obtain these characteristics synthesizing periodic structures or unit cells [9], where depending on the wavelength and the size of the structure, it can be obtained a single negative (SNG), where either the permittivity or the permeability have negative values, or double negative material (DNG), where both permittivity and permeability have negative values [10], [11].

Since it was theorized the existence of negative permittivity and permeability in [12], many efforts has been made to understand and apply this physical phenomenon. It was not until the studies made on [13] that shown the first experimental results by using structures composed by copper wire strips and split ring resonators (SRR), achieving negative refraction index. This opened new possibilities in the optical, millimetric, and the microwaves regime, due to the fact that the interaction of the electromagnetic parameters ε and μ do not necessarily depend on the response of the atoms or molecules individually, but of the composite structure whose size is smaller than the wavelength [7]–[11], [13].

Several studies show that many analytical forms have been proposed to date to extract the constitutive parameters of different types of metamaterials [14]–[18]. For example, in [14], a process of homogenization is proposed for the case of multilayer periodic structures, achieving as a result, a space of tensors which describe a specific homogenous medium. In [15], a procedure which is capable of extracting effective bianisotropic parameters for reciprocal metamaterials is proposed. Finally, in [18] is exposed an alternative way to characterize metamaterials through their surface impedance. This method takes advantage of the custom design of the reflection and phase characteristics within the desired frequency band and its application (e.g. low profile antennas, waveguides). For this was used "soft" and "hard" surfaces [19], with their structure design made using computer-aided optimization techniques such as genetic algorithms [20].

One of the main purposes for the use of antennas and waveguides loaded with metamaterials is to change the propagation characteristics of the wave [21]–[35]. These changes can be seen on characteristics such as reduced cross polarization and the reduction of side lobes [36], reduction of the cutoff frequency and miniaturization [27], [37]–[42], broadband filters [41], [43], [44], and matching improvement [45]–[47]. It is for these reasons that the aerospace industry has taken interest, since they imply greater cost reduction. [48]–[50].

One way to compute the dispersion properties of waveguides and antennas with metamaterial liners is by means of the Modal Expansion Theory (MET) presented in [51], [52]; this technique is an extension of the modal theory [53] that allows to deal with anisotropic walls.

The way the MET works is by defining the structure as homogeneous anisotropic surfaces impedance walls, instead of the classic definition of a perfect electric (or magnetic) conductor structure. Recent works on this topic have dealt with the analysis of corrugated waveguides by treat them as anisotropic surface impedances [54], a systematic approach to reduce the cross-section of rectangular waveguides [55], a method to compute the dispersion properties of rectangular waveguides with 2D metamaterials [56], and recently, a development of a cylindrical waveguide with 2D metamaterial for different types of surface impedances [57].

In previous research [58], the issue of characterizing rectangular waveguides has been addressed through the implementation of anisotropic walls with the same surface impedance value, achieving better results than with classical rectangular guides. This time, we seek to analyze the electromagnetic properties in waveguides with anisotropic walls of different value, so that another degree of freedom is added for the calculation and subsequent design of waveguides with anisotropic walls.

Main objectives

- To characterize rectangular waveguides with different anisotropic surface impedances through the MET to then generate a final design by means of High Impedance Surfaces.

1 | Metamaterials

In the field of electromagnetics, materials can be described by their constitutive parameters as is shown in Figure 1.1, these are the permittivity ϵ (represented in the x-axis) and the permeability μ (represented in the y-axis).
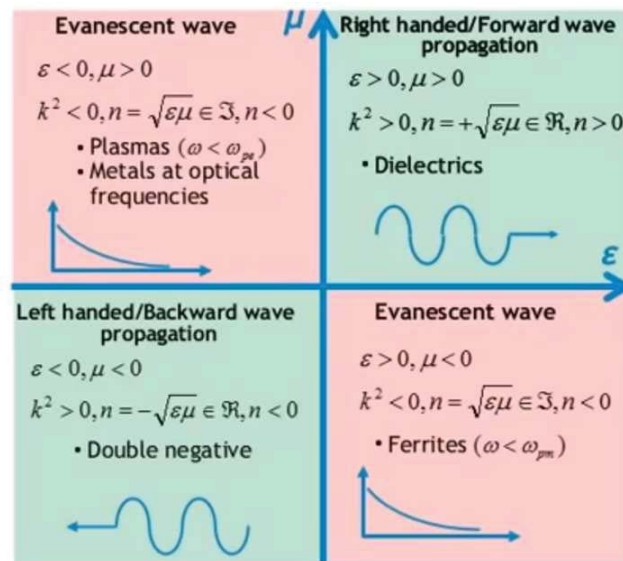

Figure 1.1: Material classification according to the constitutive parameters μ and ϵ. [59]

When both $\epsilon > 0$ and $\mu > 0$, we find materials that allow the propagation of electromagnetic waves, these materials are generally dielectric and are classified as Double Positive materials (DPS). But, if any of the constitutive parameters are negative, we are in the case where the medium does not allow the propagation of electromagnetic waves, thus the wave is called "evanescent", for example plasmas and metals at optical frequencies, where $\epsilon < 0$ and $\mu > 0$, coining the name of Epsilon Negative materials (ENG). On the other hand, we have the ferromagnetic materials, where $\epsilon > 0$ and $\mu < 0$, this type of materials are called Mu Negative materials (MNG).

The materials classified above can be found in nature, on the contrary, materials presenting the property of $\epsilon, \mu < 0$ must be engineered. These are called Double Negative materials (DNG) and have unusual characteristics, such as anti-parallel group and phase velocities, negative refractive index, and backward-wave propagation.

The concept of metamaterials is not fully established yet, but it is possible to find some definitions in common:

- They are composite materials, intentionally designed to provide properties that are not obtainable with ordinary materials.
- Its electromagnetic properties derive from its physical structure rather than its atomic structure.
- The properties they exhibit are not observable in their constituent materials.

According to the above definitions, a metamaterial must have unusual properties, so it is possible to include in this group DNG materials, Electromagnetic/Photonic Band Gap structures (EBG/PBG), Artificial Magnetic Conductors (AMC), Frequency Selective Surfaces (FSS), and High Impedance Surfaces (HIS), among many others.

When electromagnetic waves interact with such materials, they exhibit some interesting properties that can be used in order to improve the performance of microwave components and circuits, antennas, transmission lines, scatterers, and optical devices such as lenses as shown in Figure 1.2.
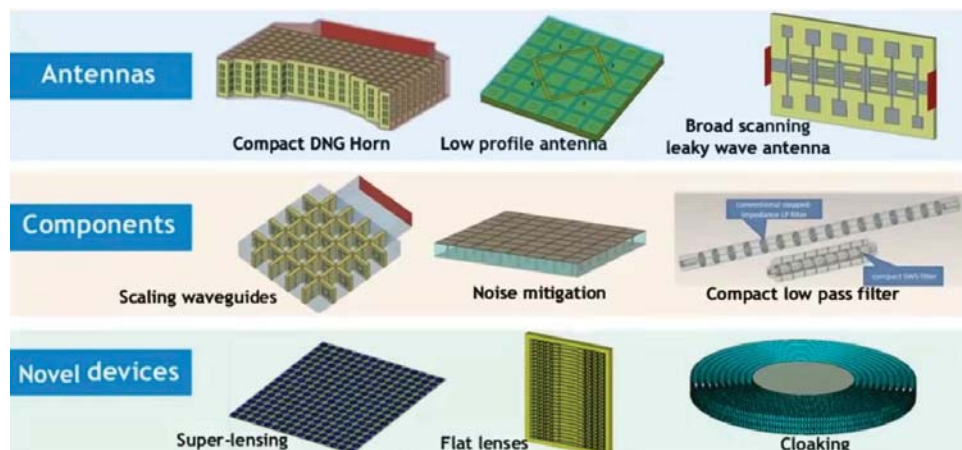

Figure 1.2: Modeling and Simulation of Metamaterial-Based Devices for Industrial Applications, CST webinar. [60]

It should be noted that these metamaterials correspond to those of the "resonant" type, this means that due to their periodicity ($< \lambda/10$), the phenomenon of dispersion of the wave does not occur. Instead, due to the existence of metallic elements, these will produce induced currents and consequently will resonate, thus emulating the resonance at an atomic scale, and thus creating waves that will combine with the main wave generating these unusual properties.

Structurally, these metamaterials are composed of periodic metallic arrangements and are much smaller than the free-space and/or guided wavelength, thus microscopically are intrinsically inhomogeneous but macroscopically they can be treated as homogeneous materials and can be represented using parameters like permittivity a permeability.

Nowadays, new techniques and concepts in synthesis and fabrication have allowed the construction of structures and composite materials that can mimic known material responses or that can give new physically realizable response functions that do not occur or may not be available in nature. These metamaterials can be synthetized by embedding various constituents/inclusions with novel geometric shapes and forms in some host media as in Figure 1.3.
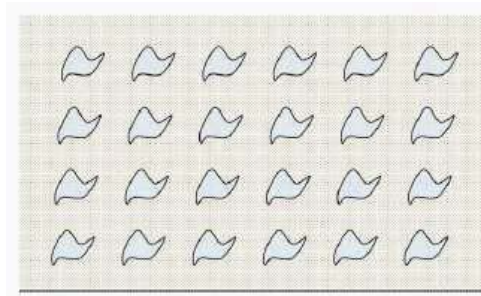
Figure 1.3: Generic sketch of a volumetric metamaterial synthesized by embedding various inclusions in a host medium. [59]

When electromagnetic waves interact with these inclusions, induction and magnetic moments appear, which in turn affects the macroscopic effective permittivity and permeability of the entire medium. For this reason, the engineers are able to tailor these inclusions in a host medium or host surface, providing independents "degrees of freedom" (like size, shape, and composition of the inclusions) in order to engineer a metamaterial with specific electromagnetic response functions not found in the individual constituents.

1.1 High Impedance Surfaces

Generally, when it is desired to reflect or isolate the electromagnetic field emitted by an antenna, conventional dielectric media (such as those in the 1st quadrant of Figure 1.1) are the simplest option, as a ground plane. This type of reflector improves the power of the antenna in approximately 3 dB but are dependent on the proximity in which the antenna and the reflector are placed. If the distance is very small, reflected waves will be created that will cancel out with the incident wave, affecting in consequence the transmitted wave.

The solution to this problem is to place the antenna at a distance of $\lambda/4$ from the reflector, but this approach is not convenient if space is a factor in the design.

Another problem occurs due to the appearance of surface waves which are linked to the interface between the free space and the conductor [62], at microwave frequencies are generally known as surface currents, and if the surface is not perfectly smooth, has discontinuities or folds, will generate vertical radiation. In the ground plane this radiation appears at the edges and consequently interferes with the transmitted signal and can be seen as "speckles" in the radiation pattern. And if the ground plane is shared by other antennas, surface currents will generate coupling between them.

One way to mitigate or cancel out these unwanted effects is by using "High Impedance Surfaces", these structures are compounded by a "Frequency Selective Surfaces" (FSS) which is grounded by a dielectric bar. Their main characteristics are the high impedance they have within one or more frequency ranges, their reflection coefficient is +1 when they are illuminated by a plane wave unlike the Perfect Electric Conductors (PEC) that have a reflection coefficient of -1 on its surface. These structures are also capable of blocking surface waves by means of metal vias that connect the FSS with the ground plane; in this configuration they are called "Electromagnetic Band Surfaces" (EBG). A basic configuration of an a HIS is shown in Figure 1.4

AMC behavior:
normal reflection phase =
0° at resonant frequency

EBG behaviour:
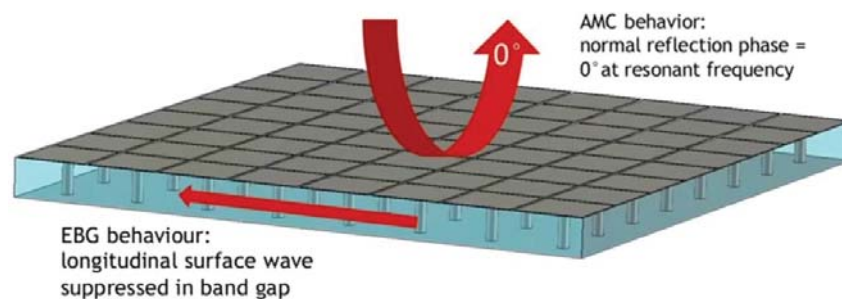longitudinal surface wave
suppressed in band gap

Figure 1.4: Basic structure of a HIS. [60]

The applications of the HIS range from ultra-thin electromagnetic absorbers [63], [64], low profile antennas [65], [66], Fabry-Perot or Leaky wave antennas [67], [68], reduction of switching noise in PCB circuits [69], [70], getting to be included in the area of metamaterials, coining

the name of metascreens [71].

Figure 1.5 shows the typical response of an HIS, where when approaching from a frequency lower than resonance, it has an inductive impedance that increases exponentially until the resonance (which in this case is 15 GHz), and then it passes to a capacitive impedance reducing in the same way.
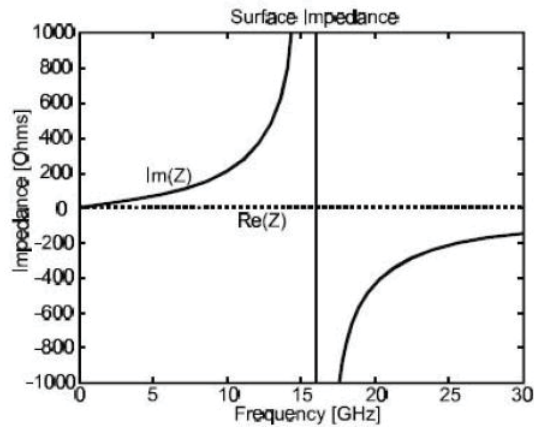

Figure 1.5: Typical response of a HIS. [61]

The engineer can handle this response according to his needs, for example, by moving the resonance frequency by varying the parameters of the structure such as the distance between the ground plane and the FSS, or even modifying only the FSS.
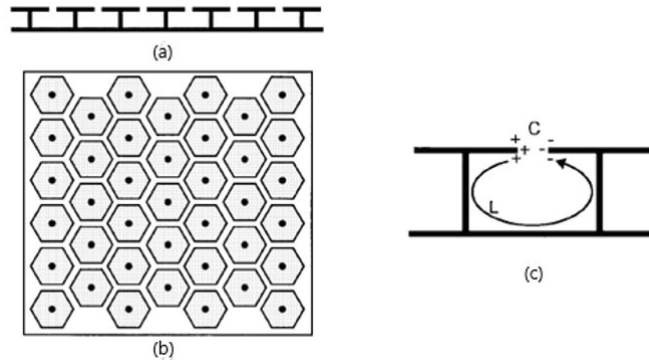
1.2 Frequency Selective Surfaces

Figure 1.6: Hexagonal mushroom-like structure (a) cross view, (b) top view, (c) analytical model. [72]

There are many geometries which offer different characteristics. The mushroom-like structure presented in [72] was one of the first to be studied. This structure presented in Figure 1.6 can be modeled by an LC equivalent network. The resonance of this structure can be controlled by modifying the effective capacitance and the effective inductance, which depend on the parameters of the geometry.

The patch type structure shown in Figure 1.6 can achieve lower resonances by designing larger patches and at the same time, reducing the spacing between the unit cells which increases the capacitance. However, this type of HIS does not have good immunity to the variations of the angle of incidence because the FSS covers almost completely preventing the passage of the wave through the substrate.

Other structures that have a better stable resonance with respect to the angle of incidence are the "meander-line based HIS" [73] presented in Figure 1.7. This type of structure is more transparent to the incident waves, in comparison to the mushroom type structure.

Figure 1.7: Several self-resonant grid structures. [61]

Another type of structure is the Hilbert curve, which is also of the self-resonant type [74]. This type of structure consists of a long wire compacted within a small space. This structure has the characteristic of resonating depending on the N order of the Hilber curve. It is also known that its resonance and bandwidth is affected by the height of the surface on the ground rather

than by the separation between adjacent elements [75]. Figure 1.8 shows the Hilber structure for different N commands
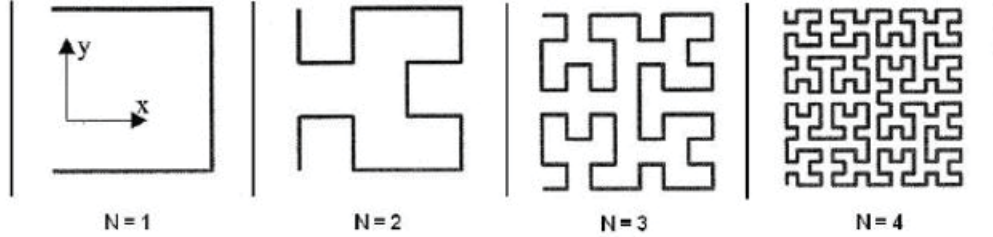

Figure 1.8: Several Hilbert curves for various iterations of order N. [61]

The use of numerical algorithms has also allowed finding structures that fit certain parameters. Such is the case of the genetic algorithms introduced in [76], which generate optimal multiband fractal structures, examples of these structures can be seen in Figure 1.9.
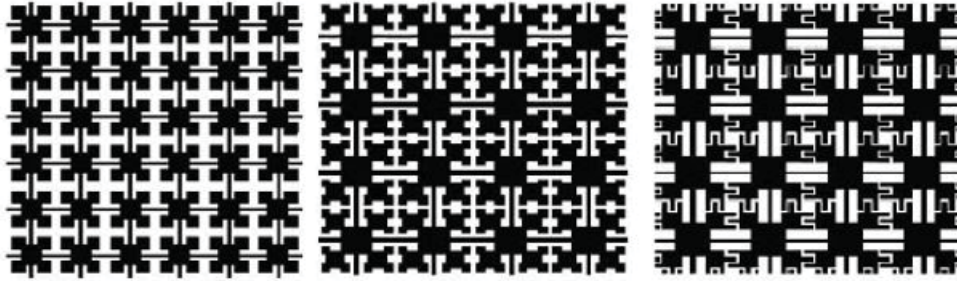

Figure 1.9: Several fractal HIS structures. [61]

1.3   Anaytical models

There are three analytical models that try to describe the behavior of the mushroom HIS, these models are used depending on the type of FSS used.

The first one was presented by Sievenpiper in [72]. This model considers the mushroom type structure (seen in Figure 1.6 as an equivalent network with parallel capacitance and inductance elements. The capacitance is due to the narrow space between the two metallic patterns on the upper surface and the results of the inductance of the metal cylinder (called "via") that connects the upper surface to the ground plane at the bottom. Its surface impedance is modeled by the following equation:

$$Z_z(\omega) = \frac{j\omega L}{1 - \omega^2 LC}$$

Where ω is the angular frequency of operation, L the inductance and C the capacitance.

The second model presented in [77] sees the HIS as a transmission line which is composed of several layers. The first layer composed of the substrate with peridic vias can be seen as the wire grid model, the second layer, composed of the periodic metal elements can be described as a homogeneous impedance surface that behaves as a capacitive or inductive grid within certain range of frequencies. Figure 1.10 shows the structure next to the transmission line model.
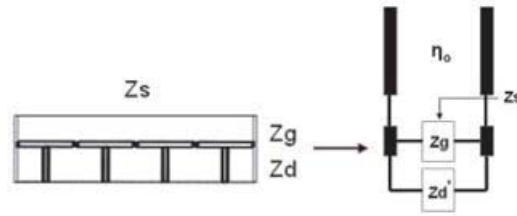

Figure 1.10: Transmission line model. [61]

Thus, the surface impedance Z_s is obtained as a parallel connection of the grid impedance Z_g and the grounded dielectric slab impedance Z_d:

$$Z_s = \frac{Z_g Z_d}{Z_g + Z_d}$$

The third model presented in [78] is an improvement from the previous one, where more accuracy is taken for oblique incidence angles by accounting the periodicity of one of the tangential directions. This model uses the transmission line approach, averaged boundary conditions, and the approximate Babinet principle. For a mushroom-like structure the analytical solutions are as follows:

$$Z_s{}^{TE} = \frac{j\omega\mu\dfrac{\tan(\beta h)}{\beta}}{1 - 2k_{eff}\alpha\dfrac{\tan(\beta h)}{\beta}\left(1 - \dfrac{1}{\epsilon + 1}\sin^2\theta\right)}$$

$$Z_s{}^{TM} = \frac{j\omega\mu\dfrac{\tan(\beta h)}{\beta}\cos^2\theta_2}{1 - 2k_{eff}\alpha\dfrac{\tan(\beta h)}{\beta}}$$

The previous analytical models falls when more complicated structures are designed, however,

numerical methods have been introduced, which use periodic boundary conditions (PBC) allowing for the design analysis quite straightforward. Some of these include finite element method (FEM), method of moments (MoM), finite difference time domain method (FDTD), and the integral equation (boundary element) method (IEM/BEM) [76], [79]–[83].

1.4   Asymmetrical High Impedance surfaces

Many applications using artificial magnetic conductors (AMC) use symmetric structures as selective frequency surfaces (FSS), in [84] the effect of using asymmetric structures is investigated, alluding to the term of polarization-dependent electromagnetic band gap or PDEBG. A PDEBG structure can provide different types of polarization depending on the asymmetric FSS used, for example, when a RHCP normally impacts on this structure, depending on the frequency, the reflected wave will not change its polarization to an LHCP, or for another frequency, the reflected wave will change to a linear polarization (LP) or an elliptical polarization (EP). Figure 1.11 shows an example of a asymmetrical FSS used to obtain a asymmetrical HIS.
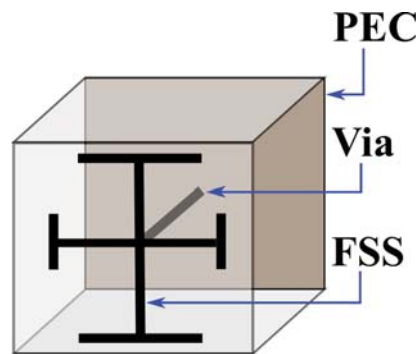

Figure 1.11: Asymmetrical HIS.

According to the above, what is the difference between a metamaterial, a HIS or a FSS?

Following the idea that metamaterials are all those materials that possess their properties by the way they are manufactured rather than by their atomic composition, HIS are structures that are composed by FSS (which act as AMC, but are just a specific condition) and another structure (usually a bias between the FSS and the ground plane) that functions as EBG within a certain frequency range. These separate structures are not able to achieve what they do as a whole, so it can be said that the HIS fit within the category of metamaterials.

2 | Rectangular waveguides

Rectangular waveguides represent a significant section of RF systems and are one of the earliest types of transmission lines that still being used to transport microwave signals. The benefits of these types of components are their high-power capability, millimeter wave applications, satellite systems and some precision test applications. A cross section of the waveguide is shown on Figure 2.1, and depending on the dimensions "a" and "b" the waveguide will propagate different modes for a frequency of operation. The type of modes that can propagate are TM (Transversal Magnetic), TE (Transversal Electric) but not TEM (Transversal ElectroMagnetic) because there is only one material present.

In the following sections, the equations that model the electromagnetic fields within a waveguide will be presented and developed following the classical theory. Later we will analyze the equations that model a waveguide with metamaterials using the Modal Expansion Theory (MET).
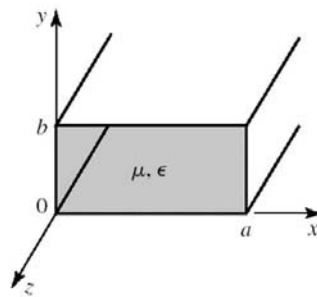

Figure 2.1: Rectangular waveguide with PEC walls. [85]

2.1 Maxwell equations

Maxwell's equations are a description of the behavior and the relation of magnetic and electric fields, charges, and currents associated with electromagnetic waves that are governed by physics laws. These laws were discovered through many years of research by many people to later be integrated by James Clerk Maxwell, a Scottish physicist and mathematician.

The differential form of Maxwell's equations is the most widely used representation to solve boundary-value electromagnetic problems. These equations relate field vectors, currents

densities, and charge densities at any point in space at any time.

They are written as follows:

$$\nabla \times \vec{H} = \frac{\partial \vec{D}}{\partial t} + \vec{J_e}$$

$$\nabla \times \vec{E} = -\frac{\partial \vec{B}}{\partial t} \tag{2.1}$$

$$\nabla \cdot \vec{B} = 0$$

$$\nabla \cdot \vec{D} = \rho_c$$

Where $\vec{H}$ is the magnetic field, $\vec{E}$ the electric field, $\vec{B}$ the magnetic induction vector, $\vec{D}$ the electric induction vector, $\vec{J_e}$ the electric current density vector and ρ_c the density charge.

If we assume that the medium is homogeneous, isotropic and invariant in time (with $\mu_r = 1$) the vectors $\vec{D}$ and $\vec{B}$ can be replaced as follow:

$$\vec{B} = \mu_0 \vec{H}$$

$$\vec{D} = \epsilon_0 \epsilon_r \vec{E}$$

With ϵ_0 and μ_0 the vacuum permittivity and permeability and ϵ_r the relative permittivity of the medium. Also, if there are no sources:

$$\rho_c = 0$$

$$\vec{J_e} = 0$$

Which means that equations in (2.1) can be rewritten as:

$$\nabla \times \vec{H} = \epsilon_0 \epsilon_r \frac{\partial \vec{E}}{\partial t}$$

$$\nabla \times \vec{E} = -\mu_0 \frac{\partial \vec{H}}{\partial t} \tag{2.2}$$

$$\nabla \cdot \vec{H} = 0$$

$$\nabla \cdot \vec{E} = 0$$

If equations (2.2) are in harmonic regime, the time domain equations can be transformed by using the Fourier transform:

$$\nabla \times \vec{H} = j\omega\epsilon_0\epsilon_r \vec{E}$$

$$\nabla \times \vec{E} = -j\omega\mu_0 \vec{H} \tag{2.3}$$

$$\nabla \cdot \vec{H} = 0$$

$$\nabla \cdot \vec{E} = 0$$

With ω the angular frequency. Also, if there is no variation along the z-axis, the electromagnetic fields can be described as:

$$\vec{E}(x, y, z) = \vec{A}(x, y)e^{-j\omega t}e^{jk_z z} \tag{2.4}$$

$$\vec{E}(x, y, z) = \vec{B}(x, y)e^{-j\omega t}e^{jk_z z} \tag{2.5}$$

Where $\vec{A}$ and $\vec{B}$ are cartesian vector functions transversals along z-axis, with k_z the waveguide number along z-axis. Thus, the electromagnetic fields have a $e^{jk_z z} = e^{\gamma_z z}$ dependency, where γ_z is the propagation constant along the z-axis.

2.2 Dispertion equation

The dispersion equation is a representation of the propagation constant along the frequency. Thanks to this, it is possible to obtain information like for example their propagative modes, their cutoff frequency (f_c) from which they will propagate, their bandwidth (the distance between two modes), the velocity group (v_g), the phase velocity (v_p) and if is right-hand or left-hand polarization. A more graphical explanation of the above is shown in Figure 2.2.

In order to obtain the dispersion equation, it is necessary to solve the partial differential equations of (2.3) to obtain at the end the "wave equation":

$$\left(\nabla^2 + k_0^2\epsilon_r\right)\vec{E} = \vec{0} \tag{2.6}$$

With, the vacuum waveguide number defined as $k_0 = \omega\sqrt{\mu_0\epsilon_0}$. Thus, equation (2.6) leads to the definition of the dispersion equation, where:

$$\gamma_z = \sqrt{k_c^2 - \epsilon_r k_0^2} = \sqrt{\left(\frac{2\pi f_c}{c}\right) - \epsilon_r k_0^2} \tag{2.7}$$
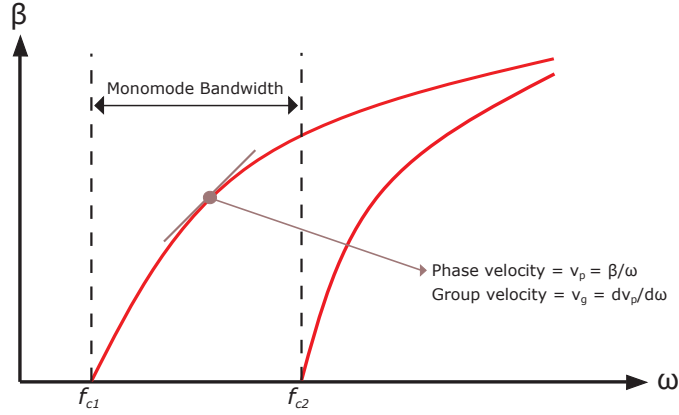
Figure 2.2: Dispersion diagram for a propagating TE or TM modes.

With $k_c = \dfrac{2\pi f_c}{c}$ and $c \approx 3 \cdot 10^8$.

For a rectangular waveguide, equation (2.7) is defined as:

$$\gamma_z = \sqrt{\left[\left(\frac{n\pi}{a}\right)^2 + \left(\frac{m\pi}{b}\right)^2\right] - \epsilon_r k_0^2} \qquad (2.8)$$

Where a and b are the transversal dimensions of the waveguide, $n, m \in \aleph$ which define the mode propagating depending of the combination, and is denoted as $\gamma_{z,mn}$.

2.3 Redefinition of the electromagnetic fields

It is possible to redefine the electromagnetic fields in transversal and longitudinal components as follows:

$$\vec{E} = \vec{E_T} + E_z \vec{z}$$

$$\vec{H} = \vec{H_T} + H_z \vec{z} \qquad (2.9)$$

$$\nabla = \nabla_T + \partial_z \vec{z} = \nabla_T - \gamma_z \vec{z}$$

With T denoting the transverse components x and y.

By using (2.3) and the definitions of (2.9), one can define the transversal fields as a function of

the longitudinal fields as:

$$\overrightarrow{E_T} = \frac{1}{k_c^2} \left(-\gamma_z \nabla_T E_z - j\omega\mu_0 \nabla_T H_z \times \overrightarrow{z} \right) \tag{2.10}$$

$$\overrightarrow{H_T} = \frac{1}{k_c^2} \left(j\omega\epsilon \nabla_T E_z \times \overrightarrow{z} - \gamma_z \nabla_T H_z \right) \tag{2.11}$$

With $k_c = \frac{2\pi f_c}{c} = \sqrt{\gamma_z^2 + k_0^2 \epsilon_r}$ the cutoff constant.

2.4 Modes of propagation

TE_{mn} Mode

When a TE (Transversal Electric) mode propagates, $E_z = 0$ and $H_z \neq 0$. For this mode, $m, n = 0, 1, 2 \dots$. But the TE_{00} mode does not exist because this will imply that the transversal fields are zero. Thus, the first mode that propagates (dominant mode) for this case is the TE_{10} (only if $a \geq b$ is defined, otherwise it will be the TE_{01}).

TM_{mn} Mode

When a TM (Transversal Magnetic) mode propagates, $E_z \neq 0$ and $H_z = 0$. For this mode, $m, n = 1, 2, 3 \dots$. Similarly, the TM_{00}, TM_{01} or TM_{10} mode does not exist because this will imply that the transversal fields are zero. Thus, the first mode that propagates (dominant mode) for this case is the TM_{11}.

TEM Mode

In this case $E_z = H_z = 0$ and $k_c = 0$, which means that it can propagate from frequency zero and with propagation constant $\gamma_z = jk_0\sqrt{\epsilon_r}$. In order for this mode to exist, two conductors should be in the waveguide with a differential potential, thus in a metallic waveguide this mode is not supported.

Hybrid mode

Lastly, when a hybrid mode exists, their longitudinal fields $E_z \neq 0$ and $H_z \neq 0$. It has been demonstrated that this propagating mode is exists with anisotropic surfaces in [51].

2.5   Mode Impedance definition

The admittance (or impedance if we take the inverse) of an electromagnetic wave relates the transversal components of the electric and magnetic field in the direction of propagation. For example, if a TEM wave travels through a homogeneous medium, the admittance (or impedance) will be equal to that of the medium across its entire length. A particular case can be an electromagnetic wave traveling in the vacuum, where the impedance of the wave will be the vacuum impedance ($Z_0 \approx 377\Omega$), mathematically the admittance Y^M of the mode "M" is defined as:

$$Y^M \overrightarrow{E_T} = \overrightarrow{H_T} \times \overrightarrow{z}$$

Where $\overrightarrow{E_T}$ and $\overrightarrow{H_T}$ are the electric and magnetic transversal components to the direction of propagation $\overrightarrow{z}$. Similarly, it is possible to use the Impedance Z^M as:

$$\overrightarrow{E_T} = Z^M \left(\overrightarrow{H_T} \times \overrightarrow{z} \right)$$

And is defined as:

$$Z^M = \frac{1}{Y^M}$$

Depending of the mode propagating, the impedance will be redefined in vacumm as:

$$Z^{M,TE} = \frac{j\omega\mu_0}{\gamma_z}$$

$$Z^{M,TM} = \frac{\gamma_z}{j\omega\epsilon_0}$$

$$Z^{M,TEM} = \sqrt{\frac{\mu_0}{\epsilon_0}}$$

For a propagating mode where $\gamma_z = j\beta_z$ the impedance will be resistive (which means it carries energy), for an evanescent mode $\gamma_z = \alpha_z$ (which means the wave is reactive). For a TM mode, the impedance is capacitive $Z = 1/(j\omega C)$ and inductive for a TE mode $Z = j\omega L$. The impedance for a TEM is always resistive.

An in-depth analytical explanation of hybrid modes can be found in [52].

2.6 Surface Impedance definition

In order to only introduce about the subject, only the mathematical concept of surface impedance will be addressed lightly.

The anisotropic surfaces in reality have volume, they are also dependent on the frequency, the angle of incidence of the wave and have dispersive properties, therefore, to characterize them it is necessary and simple to use their surface impedance.

2.6.1 Mode TE

Figure 2.3 shows a TE plane wave incident with a θ angle on an impedance surface Z_s in the Ω plane. This wave travels obliquely and is composed of an incident electromagnetic field ($\overrightarrow{E_i}$, $\overrightarrow{H_i}$ and $\overrightarrow{k_0}$) and reflected ($\overrightarrow{E_r}$, $\overrightarrow{H_r}$ and $\overrightarrow{k_0}$).

The surface impedance definition Z'_s is established as the relation between the electric field $\overrightarrow{E}$ and the magnetic field $\overrightarrow{H}$ at the level of the Ω' plane, and it is formulated as:

$$\overrightarrow{E}\Big|_{\Omega'} = Z'_s \left(\overrightarrow{H}\Big|_{\Omega'} \times \overrightarrow{n} \right) \tag{2.12}$$

Where $\overrightarrow{n}$ is the vector normal to the surface, for the case of Figure 2.3, $\overrightarrow{n} = \overrightarrow{x}$.

By developing (2.12) is possible to obtain the definition of the transversal surface impedance Z'_t at height "h" as:

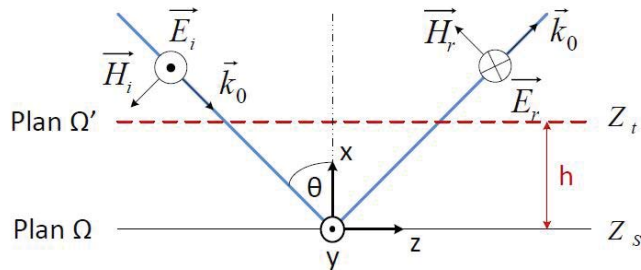$$Z'^{TE} = \frac{E_y}{H_z}\bigg|_{x=h} \tag{2.13}$$

Figure 2.3: Transmission and reflection of a TE plane wave on an impedance surface Z_s in the Ω plane. [52]

2.6.2 Mode TM

Figure 2.4 shows a TM plane wave incident with a θ angle on an impedance surface Z_s in the Ω plane. This wave travels obliquely and is composed of an incident electromagnetic field ($\overrightarrow{E_i}$,

$\overrightarrow{H_i}$ and $\overrightarrow{k_0}$) and reflected ($\overrightarrow{E_r}$, $\overrightarrow{H_r}$ and $\overrightarrow{k_0}$).

Same procedure as before, by using (2.12) and accounting for the incident an reflected electromagnetic fields, one can derive the definition of a longitudinal surface impedance Z'_z at height "h" as:

$$Z'^{TM} = -\frac{E_x}{H_y}\bigg|_{x=h} \tag{2.14}$$

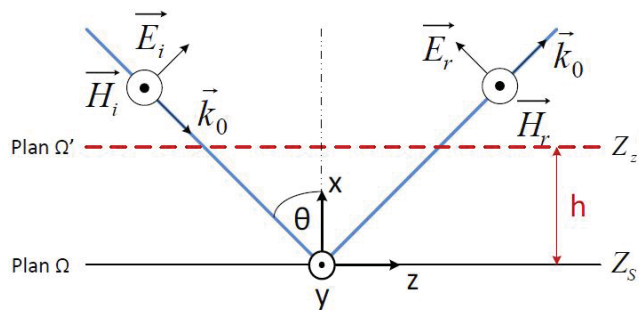The equations (2.13) and (2.14) will be used for the next chapter.

Figure 2.4: Transmission and reflection of a TM plane wave on an impedance surface Z_s in the Ω plane. [52]

From now on and to facilitate understanding, the definitions of transverse and longitudinal surface impedances will be redefined as $Z'^{TE} = Z'_t$ and $Z'^{TM} = Z'_z$.

3 Anisotropic waveguides

This theoretical part constitutes an improved study of [58]. In this previous work, the MET proved to calculate with accuracy and quickly the γ propagation constant for conventional and anisotropic metamaterial walls waveguides (with same properties on the two parallel walls).

In Figure 3.1, the boundary conditions are redefined to deal with different parallel anisotropic walls. The horizontal walls ($y = 0$ and $y = b$) are still Perfect Electric Conductors (PEC) and the vertical walls ($x = -a$ and $x = a$) present different conditions along the two directions as expressed in (3.1) and (3.2).
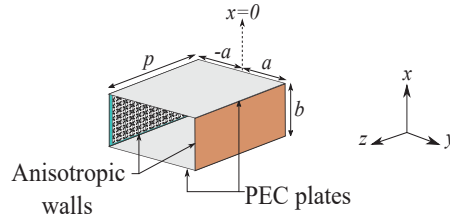
Figure 3.1: Rectangular waveguide with anisotropic walls.

3.1 Boundary conditions

The following equations express the anisotropic conditions at the vertical walls for a rectangular waveguide:

$$Z_{t1} = \left.\frac{E_y}{H_z}\right|_{x=-a}, \; Z_{t2} = -\left.\frac{E_y}{H_z}\right|_{x=a} \tag{3.1}$$

$$Z_{z1} = -\left.\frac{E_z}{H_y}\right|_{x=-a}, \; Z_{z2} = \left.\frac{E_z}{H_y}\right|_{x=a} \tag{3.2}$$

Z_{t1} and Z_{t2} are the transversal impedances, and Z_{z1} and Z_{z2} are the longitudinal impedances. These impedances might be complex to include losses, although in the following development

only purely imaginary surface impedances are considered. The boundary conditions on the horizontal walls ($y = 0$ and $y = b$), are still the following:

$$E_z|_{y=0} = E_z|_{y=b} = 0 \tag{3.3}$$

$$\left.\frac{\partial H_z}{\partial y}\right|_{y=0} = \left.\frac{\partial H_z}{\partial y}\right|_{y=b} = 0 \tag{3.4}$$

The electromagnetic fields in the direction of propagation are decomposed as incidental and reflected waves such as in [58].

$$E_z = \left(\alpha_- e^{jk_x x} + \alpha_+ e^{-jk_x x}\right)\sin(k_y y) \tag{3.5}$$

$$H_z = \left(\delta_- e^{jk_x x} + \delta_+ e^{-jk_x x}\right)\cos(k_y y) \tag{3.6}$$

where α_-, α_+, δ_- and δ_+ are unknown constants. k_x and k_y are respectively the propagation constants along x-axis and y-axis with $k_y = m\pi/b$ and m an integer.

The transversal field components in waveguides are defined by [85].

$$\overrightarrow{E_T} = \frac{1}{k_c^2}(-\gamma \nabla_T E_z - j\omega\mu_0 \nabla_T H_z \times \overrightarrow{z}), \tag{3.7}$$

$$\overrightarrow{H_T} = \frac{1}{k_c^2}(j\omega\epsilon \nabla_T E_z \times \overrightarrow{z} - \gamma \nabla_T H_z), \tag{3.8}$$

where k_c is the cutoff propagation constant, ϵ the waveguide permittivity and μ_0 the vacuum permeability.

3.2 $\alpha_-, \alpha_+, \delta_-, \delta_+$ determination.

By replacing the field equations (3.5) to (3.8) on the new boundary conditions (3.1) to (3.2), we get following matrix form:

$$[M]\begin{bmatrix} \alpha_- \\ \alpha_+ \\ \delta_- \\ \delta_+ \end{bmatrix} = \overrightarrow{0} \tag{3.9}$$

Where:

$$[M] = \begin{bmatrix} uX & u & (f+e_1)X & e_1-f \\ u & uX & -e_2+f & -(e_2+f)X \\ (g_1+h)X & -g_1+h & v_1 X & v_1 \\ g_2-h & -(g_2+h)X & v_2 & v_2 X \end{bmatrix} \tag{3.10}$$

Where $u = \gamma k_y$, $f = Z_0 k_0 k_x$, $e_1 = Z_{t1} k_c^2$, $e_2 = Z_{t2} k_c^2$, $h = Z_0 k_c^2$, $g_1 = Z_{z1} k_0 k_x$, $g_2 = Z_{z2} k_0 k_x$, $v_1 = Z_{z1} Z_0 \gamma k_y$, $v_2 = Z_{z2} Z_0 \gamma k_y$ and $X = e^{-2jk_x a}$. To find the $(\alpha_-, \alpha_+, \delta_-, \delta_+)^T$ unknown vector, the [M] eigenvector corresponding to the $\lambda = 0$ eigenvalue is to be solverd.

Furthermore, it is possible to recover the matrix presented in [58] if $Z_{z1} = Z_{z2} = Z_z$, and $Z_{t1} = Z_{t2} = Z_t$ conditions are settled and by changing reference coordinates of the x-axis.

3.2.1   Specific case, $m = 0$

When $m = 0$, $k_y = m\pi / b = 0$ and therefore $E_z = 0 = H_y$, hence the transversal electromagnetic fields are defined in equations (3.11) to (3.14).

$$E_x = 0 \tag{3.11}$$

$$E_y = -\frac{Z_0 k_0 k_x (\delta_- e^{jk_x x} - \delta_+ e^{-jk_x x})}{k_c^2} \tag{3.12}$$

$$H_x = -\frac{j\gamma k_x (\delta_- e^{jk_x x} - \delta_+ e^{-jk_x x})}{k_c^2} \tag{3.13}$$

$$H_y = 0 \tag{3.14}$$

The dispersion equation is consequently independent on Z_{z1} and Z_{z2}. Hence, (3.1) results in (3.15).

$$\begin{bmatrix} (f + e_1)X & e_1 - f \\ -e_2 + f & -(e_2 + f)X \end{bmatrix} \begin{bmatrix} \delta_- \\ \delta_+ \end{bmatrix} = \vec{0} \tag{3.15}$$

which is a reduced form of the matrix equation presented in (3.9). It should be noted that this last equation is also the one to solve when $Z_{z1} = Z_{z2} = 0$.

4 Results

4.1 Configuration of HFSS

A series of tests detailed in table 4.1 are performed by varying the surface impedances to firstly validate the method by comparison with the commercial software ANSYS HFSS [86] results, and secondly to analyze the structure sentivity to fabrication dispersion.

For this example, a WR284 waveguide (Figure 4.1) of dimension $a = 3,607\,cm$, $b = 3,404\,cm$ and $p = 0,01\,cm$ is taken as reference.

The boundary conditions for the left and right side walls are the anisotropic impedances of table 4.1, the top and bottom walls have PEC conditions and the front and back walls have master-slave boundaries conditions.
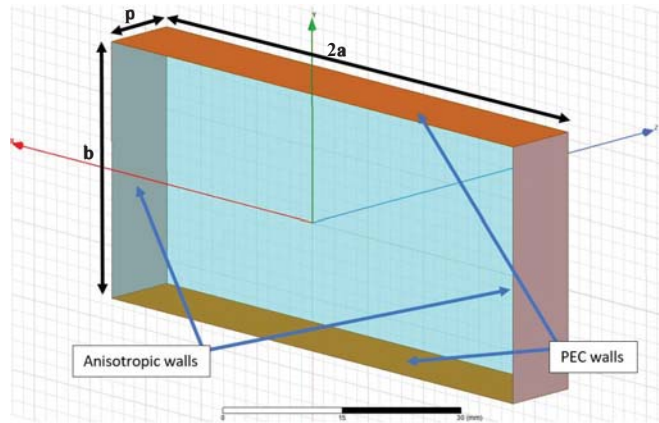
Figure 4.1: Anisotropic rectangular waveguide model tested in Ansys HFSS [86].

The Eigenmode solver is used to compute the dispersion diagrams, since the β propagation constant is a function of the phase shift between the two periodic walls. Phase variation from $0°$ to $180°$ leads to the dispersion diagram plots with (4.1).

$$\beta = \frac{\angle S_{21}}{p} \tag{4.1}$$

where $\angle S_{21}$ is the phase difference between the two periodic walls and p is the distance

between the periodic walls.

Because it is necessary to find the modes propagating within a frequency range, the Eigensolver must be configured in advance. This is why the phase constant or k_0's is defined for each mode that is found, mathematically described by equation (4.2) as:

$$k_{0(Mode(i))} = \frac{2\pi Re[Mode(i)]}{3 \cdot 10^8} \tag{4.2}$$

Where $k_{0(Mode(i))}$ is the phase constant for the Mode "i", and $Re[Mode(i)]$ is the real part of the frequency which is an output quantity defined in the analysis setup. Finally, dispersion diagrams are plotted through their effective permittivity with (4.3) for each mode [85].

$$\epsilon_{eff(Mode(i))} = \left(\frac{\beta}{k_{0(Mode(i))}}\right)^2 \tag{4.3}$$

Table 4.1 shows the studied cases for different values of anisotropic walls. The equations (3.9) and (3.15) are applied in the algorithm presented in [51].

Table 4.1: Anisotropic Cases

Case n°	Z_{z1}	Z_{z2}	Z_{t1}	Z_{t2}
1		PEC		
2	jZ_0	jZ_0	jZ_0	jZ_0
3	$1.1jZ_0$	$0.9jZ_0$	jZ_0	jZ_0
4	jZ_0	jZ_0	$1.1jZ_0$	$0.9jZ_0$
5	$1.1jZ_0$	$0.9jZ_0$	$1.1jZ_0$	$0.9jZ_0$
6	$1.1jZ_0$	$0.9jZ_0$	$0.9jZ_0$	$0.9jZ_0$
7	$0.9jZ_0$	jZ_0	jZ_0	jZ_0
8	$1.1jZ_0$	jZ_0	jZ_0	jZ_0
9	jZ_0	jZ_0	$0.9jZ_0$	jZ_0
10	jZ_0	jZ_0	$1.1jZ_0$	jZ_0

4.2 Dispersion plot results, cases 1 to 10

These results are compared HFSS results in Figure 4.2, for each case a good agreement between the MET and HFSS results is observed.
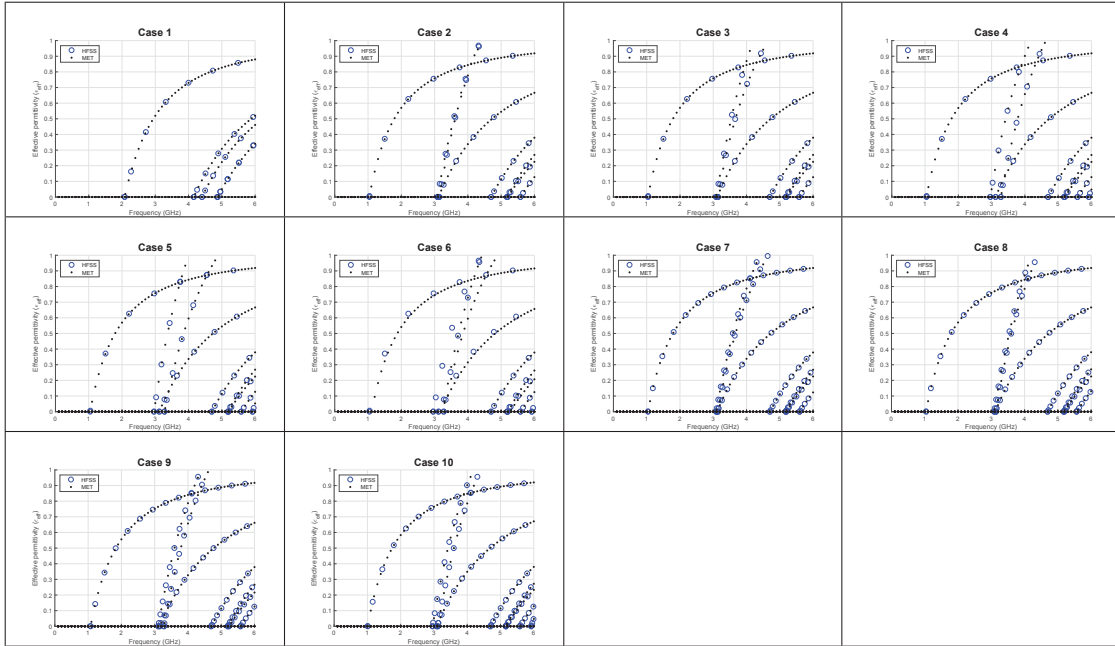

Figure 4.2: MatLab and HFSS courves of Epsilon effective (ϵ_{eff}) as function of frequency for different anisotropic wall impedances exposed on Table 4.1

.

In Table 4.2, the electromagnetic characteristics of each case is recalled. For the sensitivity test, case 2 is chosen as reference since it corresponds to a case known and studied in [56] as well as serving as a starting point by allowing to independently vary Z_{z1}, Z_{z2}, Z_{t1} and Z_{t2}.

The purpose of these cases is to perform a sensitivity analysis on the walls of the surface impedance, for this, the values of the anisotropic walls are modified in small increments to see the effects in the previous dispersion diagram, reflecting the relevant information in the Table 4.2 consequently.

According to Table 4.2 results, an increase of one transverse impedance above the case 2 transverse impedance reference (such as in case 10) leads to lower the fundamental mode cutoff frequency. This result can be exploited since it implies that the waveguide can work at lower frequencies but maintaining its size, requiring only the variation of the transverse impedance (Z_t) in one of the walls.

Table 4.2: Summary of the different cases

Case n°	f_c (1st mode) (GHz)	f_c (2nd mode) (GHz)	BW (GHz)
2	1.04	3.09	2.04
3	1.04	3.09	2.04
4	1.05	2.96	1.91
5	1.05	2.96	1.91
6	1.05	2.96	1.91
7	1.04	3.09	2.05
8	1.04	3.09	2.05
9	1.07	3.11	2.03
10	1.01	2.96	1.95

fc = Cutoff frequency

Bw = fc(2nd mode) - fc(1st mode)

Additionnal tests are therefore proposed around cases 9 and 10 to find a lower cutoff frequency, as it varies Z_{t1} between $0.2\,j\,Z_0$ to $2.5\,j\,Z_0$.

4.3 Dispersion plot results, cases around Z_{t1}

Table 4.3 shows the new cases around Z_{t1}.

Table 4.3: Anisotropic Cases around Z_{t1}

Case n°	Z_{z1}	Z_{z2}	Z_{t1}	Z_{t2}
9e	jZ_0	jZ_0	$0.2jZ_0$	jZ_0
9d	jZ_0	jZ_0	$0.4jZ_0$	jZ_0
9c	jZ_0	jZ_0	$0.6jZ_0$	jZ_0
9b	jZ_0	jZ_0	$0.7jZ_0$	jZ_0
9a	jZ_0	jZ_0	$0.8jZ_0$	jZ_0
9	jZ_0	jZ_0	$0.9jZ_0$	jZ_0
2	jZ_0	jZ_0	jZ_0	jZ_0
10	jZ_0	jZ_0	$1.1jZ_0$	jZ_0
10a	jZ_0	jZ_0	$1.5jZ_0$	jZ_0
10b	jZ_0	jZ_0	$2jZ_0$	jZ_0
10c	jZ_0	jZ_0	$2.5jZ_0$	jZ_0

Taking as reference the characteristics of bandwidth and fundamental cutoff frequency of case 2 in table 4.4: when Z_{t1} ranges from jZ_0 to $0.2jZ_0$, the fundamental cutoff frequency is shifted to higher frequencies together with a decrease in bandwidth, which can be reduced up to a 17.6% as is shown in case 9e of $\triangle$Bw. On the other hand, an increase of Z_{t1} from jZ_0 to $2.5jZ_0$, implies a reduction of the cutoff frequencies of the fundamental mode but at the cost of reducing the bandwidth drastically up to a 57.72% as in the case 10c. Finally, when the impedance difference is more significant ($Z_{t1} > 2.5jZ_0$), hybrid modes starts propagating on the waveguide.

Table 4.4: Summary of the different cases around Z_{t1}

Case n°	f_c (1st mode) (GHz)	f_c (2nd mode) (GHz)	BW (GHz)	$\triangle BW$ (%)	$\triangle f_c$ (%)
9e	1.43	3.11	1.68	-17.56	0.38
9d	1.31	3.11	1.80	-11.66	0.26
9c	1.20	3.11	1.91	-6.50	0.16
9b	1.16	3.11	1.96	-4.25	0.11
9a	1.11	3.11	2.00	-2.23	0.07
9	1.07	3.11	2.03	-0.46	0.03
2	1.04	3.09	2.04	-	-
10	1.01	2.96	1.95	-4.60	-0.04
10a	0.91	2.44	1.53	-25.04	-0.13
10b	0.83	1.97	1.14	-44.16	-0.22
10c	0.77	1.63	0.86	-57.72	-0.27

f_c = Cutoff frequency

BW = Bandwith, f_c (2nd mode) - f_c (1st mode)

$\triangle BW$ = (BW (case n°) - BW (case 3)/BW (case 3))*100

$\triangle f_c$ = ((f_c (case n°) - f_c (case 3))/Fc (case 3))*100

Figure 4.3 represents the same information as in table 4.4; the left figure shows the bandwidth as it varies the Z_{t1} impedance. Clearly, when the transverse impedance is greater than 1 (normalized by jZ_0) the bandwidth decrease drastically.

The right figure shows the variation of the cutoff frequency as it varies the transverse impedance Z_{t1}. In this case, the cutoff frequency is greater at lower values of Z_{t1} and lower at higher values.
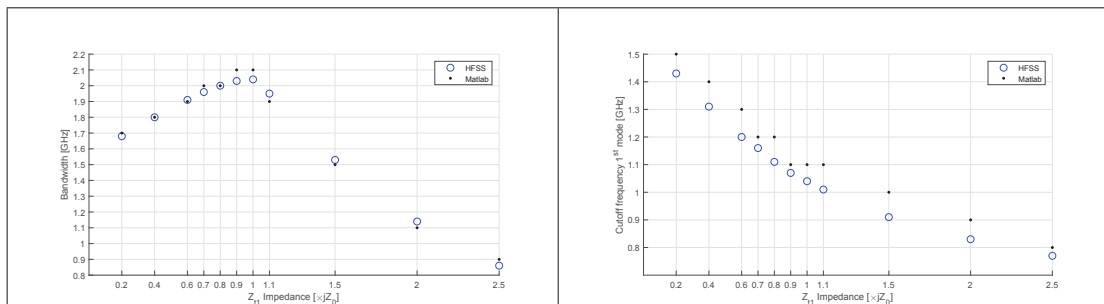
Figure 4.3: HFSS vs Matlab results, only variations in Z_{t1} according to Table 4.3.

It should be noted that these results can be compared with conventional waveguides for

the same working frequencies. This is the purpose of Table 4.5. A WR770 waveguide, can be replaced if we use a surface impedance $Z_{t1} = 2.5jZ_0$ (case 10c) in a WR284 waveguide (and assuming that the metamaterial dimensions are not considered), achieving a cross section reduction of $87, 16\%$ and a bandwidth increase of 11.2%. On the other hand, a WR650 waveguide can be replaced if this time we use a surface impedance $Z_{t1} = 1.5jZ_0$ (case 10a) in the same WR284 waveguide, achieving a cross section reduction of 81.98% and a bandwidth increase of 20.4%. Furthermore, if we consider a WR284 waveguide with any of the following impedances, $Z_{t1} = 0.9jZ_0$ (case 9), $Z_{t1} = jZ_0$ (case 2) or $Z_{t1} = 1.1jZ_0$ (case 10), these will have a reduction in their cross section of about a 29.27% with respect to the WR510 waveguide and improved bandwidths of 43.1%, 43.4% and 40.6% respectively. Same applies for these cases if the comparison is now with respect to a WR430 waveguide, it is possible to get an 41.17 cross section reduction and improved bandwidths of 32.5% (case 9), 32.8% (case 2) and 29.6% (case 10) respectively.

Finally, due to the large bandwidth of cases 9, 2 and 10, it is possible to use any of these to work simultaneously within the operating ranges of the WR430 and WR510 waveguides. A summary of the above is presented in Table 4.5.

Table 4.5: Comparisons of waveguides characteristics with respect to the anisotropic cases

Desig-nation	f_c (1st mode) (GHz)	f_c (2nd mode) (GHz)	Surf. (cm^2)	With case #	$\triangle$ Surf. (%)	$\triangle$ BW. (%)
WR284	2,08	4,16	24,56	-	-	-
WR430	1,37	2,75	59,65	2, 9 or 10	~41.17	~31,6
WR510	1,16	2,31	83,90	2, 9 or 10	~29.27	~42,4
WR650	0,91	1,82	136,29	10a	~81.98	~20,4
WR770	0,77	1,53	191,26	10c	~87,16	~11,2

$\triangle$**Surf. = surface reduction (compared to the WR284 waveguide)**

$\triangle$**BW. = bandwidth increment (when using the surf. impedance)**

Figure 4.4 shows the same information, but less clearly as table 4.5. And as before, good agreement between FEM code and Simulation can be found.
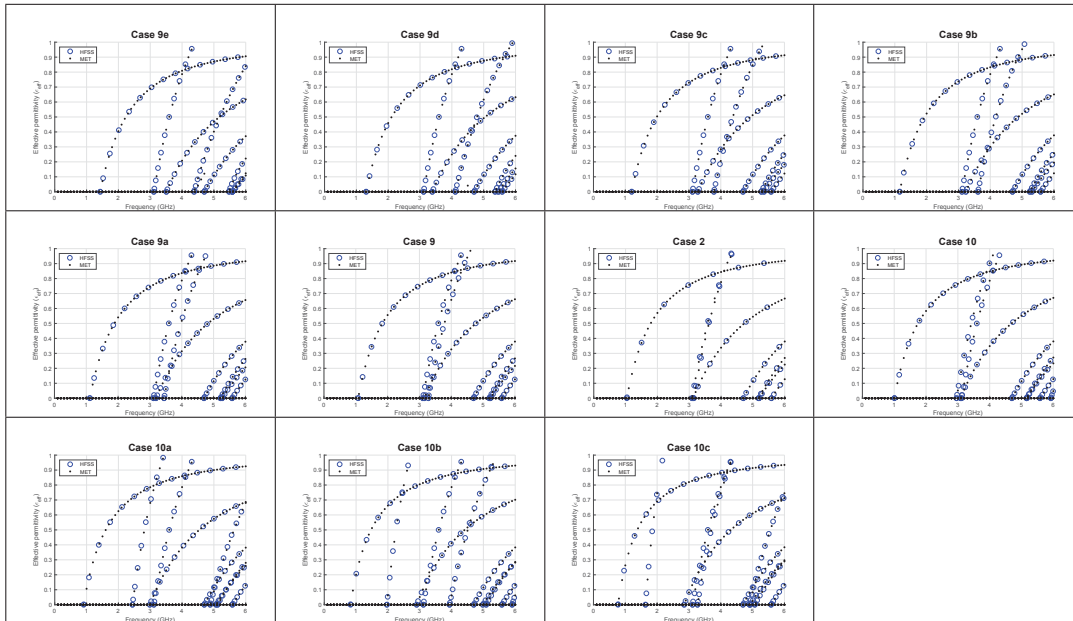
Figure 4.4: HFSS vs Matlab results, only variations in Z_{t1}.

5 Design of an High Impedance Surface

5.1 Simulation of unit cells

When it is necessary to repeat a design of some particular structure, for example an array of antennas, selective frequency surfaces, etc. These problems can be simulated using periodic boundary conditions. In HFSS this can be achieved by declaring a face as "Master" and parallel to this its "Slave" face.

There are two types of boundary conditions available in HFSS:

- Perfectly Matched Layers (PMLs):
  This type of edge simulates a fictitious material which absorbs the electromagnetic field that falls on it.
- Periodic boundary conditions - Master and Slave boundaries:
  This type of edges allow modeling planes of periodicity where the electric field of a surface fits with the electric field of another surface with a certain degree of phase shift. This type of condition is useful to simulate infinite arrays.
  Unlike a contour of symmetry, the electric field does not have to be tangential or normal to this contour, only the same magnitude and direction must be fulfilled (or the same magnitude but with opposite direction).
  Some considerations should be taken when using this type of boundary condition:
  - They can only be assigned to flat faces.
  - The geometry of a surface (for example declared as "Master") must correspond to the geometry of the surface at the other end (declared as "Slave").

Next, the steps taken in the search for high impedance surfaces that satisfy the results obtained in the previous chapter will be detailed, specifically, the search for the impedance values between the working frequencies shown in Table 4.5.

5.2 Configuration of the unit cell in HFSS

As a point of reference and to obtain practical knowledge on how to apply Floquet ports, the unit cell PIC is designed, which corresponds to the design made in [52]. As shown in Figure 5.1, it is initially designed under the parameters indicated in Table 5.1 and surface impedance
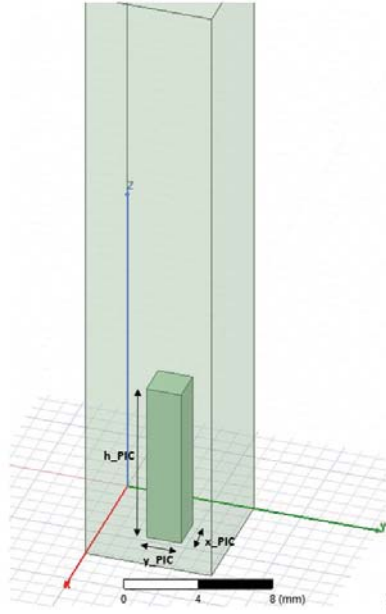
Figure 5.1: PIC [86].

Table 5.1: PIC unit cell parameters

Iteration	x_PIC	y_PIC	h_PIC
1	2	2	9.6
2	3	2	9.6
3	5	2	9.6
4	7	2	9.6
5	2	3	9.6
6	2	5	9.6
7	2	7	9.6
8	2	2	3
9	2	2	6
10	2	2	9
11	2	2	12
12	2	2	15
13	2	2	18
14	2	2	21
15	2	2	24
16	2	2	27

graphs Z_t and Z_z are obtained for each iteration, the effects can be seen when varying some of these parameters.

After analyzing the graphs of Figure C.1 and C.2 for each iteration, we observe a trend in this design which is the non-linearity of both surface impedances, since the objective is to find the constant impedance values within the frequency ranges shown in the Table 4.5. In addition, it should be noted that for reasons of time, only an evaluation of the sensitivity behavior of the structures with respect to their impedance response is made, so it is decided to take an impedance range between $0.9jZ_0$ and $1.1jZ_0$ for Z_t y Z_z and a frequency range between $1.37GHz$ and $2.75GHz$ which corresponds to the frequency of operation of a WR430 waveguide.

For the case of the PIC structure, it is possible to observe that the iterations 13 to 16 manage to reach the transverse and longitudinal impedance ranges only when modifying the height. It is also noted that this design is susceptible to the angle of incidence of the wave for the case Z_t unlike Z_z.

Table 5.2: T unit cell parameters (x-axis)
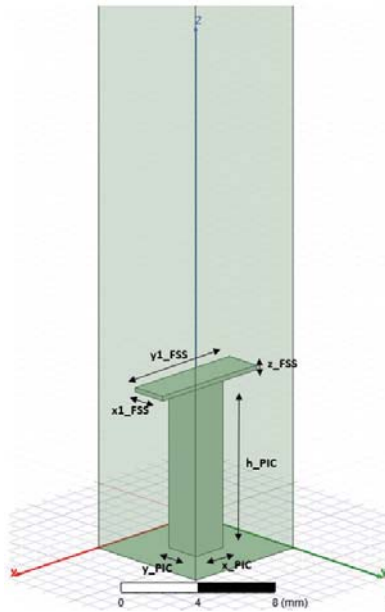
Figure 5.2: T-like unit cell [86].

Iteration	x_FSS	y_FSS	h_PIC
1	7	2	9.6
2	5.5	2	9.6
3	4	2	9.6
4	2.5	2	9.6
5	7	2.5	9.6
6	7	4	9.6
7	7	5.5	9.6
8	7	2	3
9	7	2	6
10	7	2	9
11	7	2	12
12	7	2	15
13	7	2	18
14	7	2	21
15	7	2	24
16	7	2	27
Constants			

x_PIC = y_PIC = 2

z_FSS = 0.25

For the case of the "T" structure on the x-axis presented in Table 5.2, Figure C.3 and Figure C.4 shows a change in the Z_z impedance on iterations 1 and 2. This agrees with section 1.2, where the separation between frequency selective surfaces affects the general capacitance, changing the surface impedance. Even so, only iterations 11 to 16 (which modify the height of the unit cell) are able to reach the required impedance range at the established frequency (that is, Z_t and Z_z between $0.9jZ_0$ and $1.1jZ_0$, and frequency range between $1.37GHz$ and $2.75GHz$).

Table 5.3: T unit cell parameters (y-axis)

Iteration	x_FSS	y_FSS	h_PIC
1	2	7	9.6
2	2	5.5	9.6
3	2	4	9.6
4	2	2.5	9.6
5	2.5	7	9.6
6	4	7	9.6
7	5.5	7	9.6
8	2	7	3
9	2	7	6
10	2	7	9
11	2	7	12
12	2	7	15
13	2	7	18
14	2	7	21
15	2	7	24
16	2	7	27

Constants

x_PIC = y_PIC = 2

z_FSS = 0.25
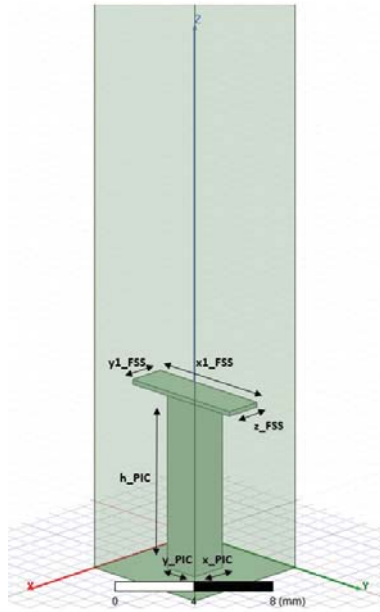
Figure 5.3: T-like unit cell [86].

Similar to the previous case, the T shaped unit cell but now parallel to the y-axis (Figure C.5 and Figure C.6) shows variation in the impedance Z_t and presents the same behavior as the previous case reaching the resonance required at iterations 11 to 16.

Table 5.4: "X" FSS unit cell parameters
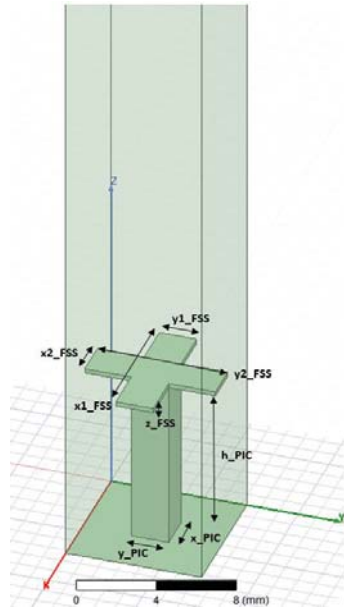
Figure 5.4: X-like unit cell [86].

Iteration	x1_FSS	y2_FSS	h_PIC
1	7	7	9.6
2	5.5	7	9.6
3	4	7	9.6
4	2.5	7	9.6
5	2.5	5.5	9.6
6	4	4	9.6
7	5.5	2.5	9.6
8	2	7	3
9	2	7	6
10	2	7	9
11	2	7	12
12	2	7	15
13	2	7	18
14	2	7	21
15	2	7	24
16	2	7	27

Constants

y1_FSS = x2_FSS = x_PIC = y_PIC = 2
z_FSS = 0.25

The X shape unit cell in Figure 5.4 shows better insensitivity to the angle of incidence for both Z_t and Z_z, which means the same values of impedance along the frequency, in addition to being able to control the slope of Z_t or Z_z when modifying the length of the arms of the surface (iterations 1 to 7). In any case, these results are not required, but it is possible to achieve them if the height is modified as in iterations 11 to 16 (Figure C.7 and Figure C.8).

Table 5.5: Jerusalem cross unit cell parameters

Iteration	y3_FSS	x4_FSS	h_PIC
1	6	6	9.6
2	6	5.5	9.6
3	6	4	9.6
4	6	2.5	9.6
5	5.5	6	9.6
6	4	6	9.6
7	2.5	6	9.6
8	6	6	3
9	6	6	6
10	6	6	9
11	6	6	12
12	6	6	15
13	6	6	18
14	6	6	21
15	6	6	24
16	6	6	27
Constants			
x1_FSS = y2_FSS = 7			
y1_FSS = x2_FSS = x_PIC = y_PIC = 2			
x3_FSS = x4_FSS = z_FSS = 0.25			
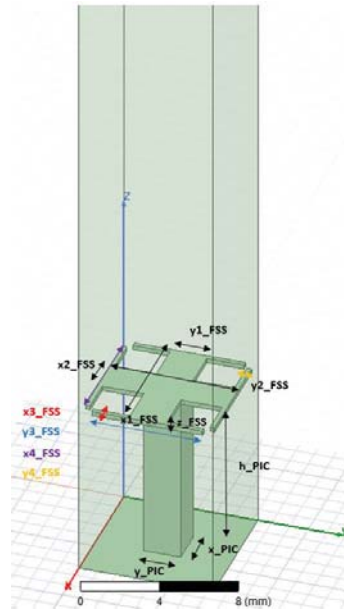
Figure 5.5: Jerusalem cross unit cell [86].

Finally, the Jerusalem cross structure of the Figure 5.5 is the one that presents the best results, being able to observe from the plots of Figure C.9 and Figure C.10 better insensibility to the angle of incidence. In addition, by varying the length of the parameters "x4_FSS" and "y3_FSS", changes in Z_t or Z_z can be observed independently, which would allow the design of the required anisotropic surface (but the non-linearity still needs to be corrected). Regarding whether it complies with the required ranges, this structure reaches the impedance values and frequency range from iterations 1 to 7, reaching almost the entire frequency range sought in iterations 11 to 16.

Due to the time, the results obtained in this section did not reach the proposed goal, which consisted in obtaining the impedance values within the ranges shown in Table 4.5. Even so, these results and procedures are left to continue the search of the unit cells.

Conclusions

Currently, research in metamaterials has allowed to open a field of electromagnetism that only existed in the theoretical world since the '60s, and the fruits of this work have materialized in new technologies for fields like optics, electronics, acoustic among others, so it is an interdisciplinary work, since it deals with composite materials that have physical properties that can exceed or complement what already exists in nature. Initially, the metamaterials were developed to modify at will the electromagnetic properties of the medium, but this concept has already been extended to include elastic, acoustic and thermal properties. Since 1999, thanks to the discovery of Pendry, the field of metamaterials has attracted all the attention of the scientific community, being able to apply in branches of antenna and waveguide engineering, imaging, sensors and light manipulation. Metamaterial research has brought together electrical engineers, material and optical scientists, chemists, and mathematicians; it has also advanced our understanding of electrodynamics, pushed the boundaries of nanofabrication, and stimulated the development of novel characterization techniques.

The definition of metamaterial is not well defined, but a term common to all branches of engineering is; artificially designed material (like composites) that offers properties not found by natural means. Metamaterials have their unusual properties thanks to the way in which their elementary blocks are organized (on a scale smaller than the wavelength of work), rather than by the individual ordering of the atoms that make them up, such as metals and dielectrics. And because of this subwavelength feature, metamaterials do not diffract light and hence are different from photonic crystals, acting as uniform media that can, in principle, as ascribed to effective refractive index.

Within the area of metamaterials, high impedance surfaces are found, these are composed by resonant cavities synthesized by printing a selective frequency surface on top of a grounded dielectric slab. These structures have the property of perfect magnetic conductor within a frequency range and for this same reason are classified as artificial magnetic conductors. The applications of this technology range from the design of ultra-thin electromagnetic absorbers, low-profile antennas, Fabry-Perot or Leaky wave antennas, to mitigate the simultaneous switching noise (SSN) in PCB circuit and other applications.There are several analytical models that try to describe the behavior of some specific structure, but now these models have been replaced by more advanced computational techniques, facilitating the development of new designs.

Waveguides were one of the earliest technologies to be developed for the propagation of electromagnetic waves at high frequencies. Their ease of construction and high-power capability are one of the reasons to investigate in this well-known technology. In past research, the issue of size reduction in rectangular waveguides has been addressed through the implementation of anisotropic walls with the same surface impedance value, achieving better results than with classical rectangular waveguides. This time, we sought to analyze the electromagnetic properties in waveguides with anisotropic walls of different value, obtaining interesting results such as the customized modification of the bandwidth or the displacement in the cutoff frequency by means of the variation of one of the transverse impedances being able to exploit this feature in the operating range of conventional waveguides with better performance. The work done here allows us to advance in the search for a unit cell by means of high impedance surfaces with the anisotropic impedance values analyzed.

Bibliography

[1] L. Rayleigh, "Xviii. on the passage of electric waves through tubes, or the vibrations of dielectric cylinders," *The London, Edinburgh, and Dublin Philosophical Magazine and Journal of Science*, vol. 43, no. 261, pp. 125–132, 1897.

[2] C. Lee, S. Lee, and S. Chuang, "Plot of modal field distribution in rectangular and circular waveguides," *IEEE transactions on microwave theory and techniques*, vol. 33, no. 3, pp. 271–274, 1985.

[3] R. D. Tompkins, "A broad-band dual-mode circular waveguide transducer," *IRE Transactions on Microwave Theory and Techniques*, vol. 4, no. 3, pp. 181–183, July 1956.

[4] A. E. Atia and A. E. Williams, "Narrow-bandpass waveguide filters," *IEEE Transactions on Microwave Theory and Techniques*, vol. 20, no. 4, pp. 258–265, Apr 1972.

[5] H. Schrank, "Polarization measurements using the septum polarizer," in *1982 Antennas and Propagation Society International Symposium*, vol. 20, May 1982, pp. 227–230.

[6] D. R. Jackson, C. Caloz, and T. Itoh, "Leaky-wave antennas," *Proceedings of the IEEE*, vol. 100, no. 7, pp. 2194–2206, July 2012.

[7] S. Zouhdi, A. Sihvola, and M. Arsalane, *Advances in electromagnetics of complex media and metamaterials.* Springer Science & Business Media, 2012, vol. 89.

[8] J. Pendry, "Electromagnetic materials enter the negative age," *Physics World*, vol. 14, no. 9, p. 47, 2001.

[9] D. R. Smith, W. J. Padilla, D. Vier, S. C. Nemat-Nasser, and S. Schultz, "Composite medium with simultaneously negative permeability and permittivity," *Physical review letters*, vol. 84, no. 18, p. 4184, 2000.

[10] R. W. Ziolkowski and E. Heyman, "Wave propagation in media having negative permittivity and permeability," *Physical review E*, vol. 64, no. 5, p. 056625, 2001.

[11] D. R. Smith, J. B. Pendry, and M. C. Wiltshire, "Metamaterials and negative refractive index," *Science*, vol. 305, no. 5685, pp. 788–792, 2004.

[12] V. G. Veselago, "The electrodynamics of substances with simultaneously negative values of and μ," *Soviet physics uspekhi*, vol. 10, no. 4, p. 509, 1968.

[13] R. A. Shelby, D. R. Smith, and S. Schultz, "Experimental verification of a negative index of refraction," *science*, vol. 292, no. 5514, pp. 77–79, 2001.

[14] E. Martini, G. M. Sardi, and S. Maci, "Homogenization processes and retrieval of equivalent constitutive parameters for multisurface-metamaterials," *IEEE Trans. Antennas Propag.*, vol. 62, no. 4, pp. 2081–2092, 2014.

[15] V. Sozio, A. Vallecchi, M. Albani, and F. Capolino, "Local bianisotropic effective parameters formulas for reciprocal metamaterials," in *Radio Science Meeting (Joint with AP-S Symposium), 2014 USNC-URSI*. IEEE, 2014, pp. 87–87.

[16] D. Sounas, N. M. Estakhri, and A. Alù, "Metasurfaces with engineered reflection and transmission: Optimal designs through coupled-mode analysis," in *Advanced Electromagnetic Materials in Microwaves and Optics (METAMATERIALS), 2016 10th International Congress on*. IEEE, 2016, pp. 346–348.

[17] M. Lapine, "Strong boundary effects in microwave metamaterial samples," in *Radio and Antenna Days of the Indian Ocean (RADIO), 2016 IEEE*. IEEE, 2016, pp. 1–2.

[18] Q. Wu, M. D. Gregory, D. H. Werner, P. L. Werner, and E. Lier, "Nature-inspired design of soft, hard and hybrid metasurfaces," in *Antennas and Propagation Society International Symposium (APSURSI), 2010 IEEE*. IEEE, 2010, pp. 1–4.

[19] P.-S. Kildal, "Artificially soft and hard surfaces in electromagnetics," *IEEE Transactions on Antennas and Propagation*, vol. 38, no. 10, pp. 1537–1544, 1990.

[20] B. Choudhury, S. Bisoyi, and R. Jha, "Emerging trends in soft computing techniques for metamaterial design and optimization," *Computers, Materials, & Continua*, vol. 31, no. 3, pp. 201–227, 2012.

[21] H. Minnett and B. Thomas, "A method of synthesizing radiation patterns with axial symmetry," *IEEE Transactions on Antennas and Propagation*, vol. 14, no. 5, pp. 654–656, 1966.

[22] P.-S. Kildal and E. Lier, "Hard horns improve cluster feeds of satellite antennas," *Electronics Letters*, vol. 24, no. 8, pp. 491–492, 1988.

[23] K. K. Chan and S. K. Rao, "Design of high efficiency circular horn feeds for multibeam reflector applications," *IEEE Transactions on Antennas and Propagation*, vol. 56, no. 1, pp. 253–258, 2008.

[24] Q. Wu, C. P. Scarborough, D. H. Werner, E. Lier, and X. Wang, "Design synthesis of metasurfaces for broadband hybrid-mode horn antennas with enhanced radiation pattern and polarization characteristics," *IEEE Transactions on Antennas and Propagation*, vol. 60, no. 8, pp. 3594–3604, 2012.

[25] Q. Wu, C. P. Scarborough, B. G. Martin, R. K. Shaw, D. H. Werner, E. Lier, and X. Wang, "A k_{u}-band dual polarization hybrid-mode horn antenna enabled by printed-circuit-board metasurfaces," *IEEE Transactions on Antennas and Propagation*, vol. 61, no. 3, pp. 1089–1098, 2013.

[26] J. G. Pollock and A. K. Iyer, "Radiation characteristics of miniaturized metamaterial-lined waveguide probe antennas," in *Antennas and Propagation & USNC/URSI National Radio Science Meeting, 2015 IEEE International Symposium on*. IEEE, 2015, pp. 1734–1735.

[27] ——, "Miniaturized circular-waveguide probe antennas using metamaterial liners," *IEEE Transactions on Antennas and Propagation*, vol. 63, no. 1, pp. 428–433, 2015.

[28] M. F. Palvig, P. Meincke, O. Breinbjerg *et al.*, "Metasurface waveguides applied to matched feeds for reflector antennas," in *2017 11th European Conference on Antennas and Propagation (EUCAP)*. IEEE, 2017, pp. 3636–3638.

[29] Z. H. Jiang and W. Hong, "Design and experiments of bandwidth-controllable broadband monopole antennas with conformal anisotropic impedance surface coatings," *IEEE Transactions on Antennas and Propagation*, vol. 66, no. 3, pp. 1133–1142, 2018.

[30] W. Fathallah, H. Sakli, and T. Aguili, "Full-wave study of rectangular metamaterial waveguides using galerkin's method," in *Systems, Signals & Devices (SSD), 2013 10th International Multi-Conference on*. IEEE, 2013, pp. 1–4.

[31] Z. H. Jiang, D. H. Werner, and P. L. Werner, "An open chiro-waveguide enabled by anisotropic impedance surfaces," in *Progress in Electromagnetic Research Symposium (PIERS)*. IEEE, 2016, pp. 3143–3143.

[32] A. Kusiek and J. Mazur, "Left-handed propagation characteristics of a dielectric and metal-loaded periodic circular waveguide," *Journal of Electromagnetic Waves and Applications*, vol. 31, no. 16, pp. 1698–1710, 2017.

[33] K. Bouras, A. Labiad, S. Chaker, and M. Bouzouad, "Emulation of metamaterial waveguide," in *Electrical Engineering-Boumerdes (ICEE-B), 2017 5th International Conference on*. IEEE, 2017, pp. 1–5.

[34] L. Pulido-Mancera, M. Imani, P. Bowen, and D. Smith, "Extracting polarizability of complementary metamaterial elements using equivalence principles," in *Engineered Materials Platforms for Novel Wave Phenomena (Metamaterials), 2017 11th International Congress on*. IEEE, 2017, pp. 268–270.

[35] A. Yelizarov, I. Nazarov, A. Skuridin, and A. Kukharenko, "Investigation of a rectangular waveguide with a magnetic wall made of mushroom-shaped metamaterial," in *Vacuum Electronics Conference (IVEC), 2017 Eighteenth International*. IEEE, 2017, pp. 1–3.

[36] C. P. Scarborough, Q. Wu, D. H. Werner, E. Lier, B. G. Martin, and R. K. Shaw, "A square dual polarization metahorn design," in *Antennas and Propagation (APSURSI), 2011 IEEE International Symposium on*. IEEE, 2011, pp. 1065–1068.

[37] J. Bai, K. Ren, Q. Chen, L. Chen, G. Zhang, and Y. Fu, "Flexible dual-frequency substrate integrated waveguide antenna based on metamaterial," in *Signal Processing, Communications and Computing (ICSPCC), 2015 IEEE International Conference on.*   IEEE, 2015, pp. 1–4.

[38] G. Oliveri, E. Bekele, M. Salucci, and A. Massa, "Transformation electromagnetics miniaturization of sectoral and conical metamaterial-enhanced horn antennas," *IEEE Transactions on Antennas and Propagation*, vol. 64, no. 4, pp. 1508–1513, 2016.

[39] J. G. Pollock and A. K. Iyer, "Below-cutoff propagation in metamaterial-lined circular waveguides," *IEEE Transactions on Microwave Theory and Techniques*, vol. 61, no. 9, pp. 3169–3178, 2013.

[40] ——, "Experimental verification of below-cutoff propagation in miniaturized circular waveguides using anisotropic ennz metamaterial liners," *IEEE Transactions on Microwave Theory and Techniques*, vol. 64, no. 4, pp. 1297–1305, 2016.

[41] M. R. Hidayat and A. Munir, "Rectangular waveguide bpf using split ring resonator metamaterials," in *Communications (APCC), 2016 22nd Asia-Pacific Conference on.*   IEEE, 2016, pp. 604–608.

[42] T. Rowe, P. Forbes, J. H. Booske, and N. Behdad, "Inductive meandered metal line metamaterial for rectangular waveguide linings," *IEEE Transactions on Plasma Science*, vol. 45, no. 4, pp. 654–664, 2017.

[43] Y. Liu and H. Ma, "A broadband bandpass rectangular waveguide filter based on metamaterials," in *Metamaterials (Meta), 2012 International Workshop on.*   IEEE, 2012, pp. 1–4.

[44] D. Ramaccia, F. Bilotti, and A. Toscano, "Angular momentum-biased metamaterials for filtering waveguide components and antennas with non-reciprocal behavior," *Proc. of Metamaterials*, pp. 250–252, 2014.

[45] A. Kumar, G. Saini, and S. Singh, "Design and simulation of metamaterial loaded substrate integrated waveguide fed patch antenna for x-band military application," in *Wireless Communications, Signal Processing and Networking (WiSPNET), International Conference on.*   IEEE, 2016, pp. 550–554.

[46] J. Chocarro, J. P. Escudero, I. Liberal, and I. Ederra, "Metamaterial enhanced slotted waveguide antenna," in *Engineered Materials Platforms for Novel Wave Phenomena (Metamaterials), 2017 11th International Congress on.*   IEEE, 2017, pp. 91–93.

[47] D. L. Pinheiro, R. M. Batalha, K. S. Medeiros, F. M. Severgnini, and E. J. Silva, "S-parameters analysis of waveguide bend with metamaterial," in *Microwave and Optoelectronics Conference (IMOC), 2015 SBMO/IEEE MTT-S International.*   IEEE, 2015, pp. 1–4.

[48] E. Lier, "Review of soft and hard horn antennas, including metamaterial-based hybrid-mode horns," *IEEE Antennas and Propagation Magazine*, vol. 52, no. 2, pp. 31–39, 2010.

[49] R. K. Shaw, E. Lier, and C.-C. Hsu, "Profiled hard metamaterial horns for multi-beam reflectors," in *Antennas and Propagation Society International Symposium (APSURSI), 2010 IEEE.* IEEE, 2010, pp. 1–4.

[50] E. Lier, R. K. Shaw, M. Cuchanski, and S. Yang, "Meta-horns improve the performance of multi-beam reflector antennas," in *Antennas and Propagation (APSURSI), 2011 IEEE International Symposium on.* IEEE, 2011, pp. 2736–2737.

[51] N. Raveu, B. Byrne, L. Claudepierre, and N. Capet, "Modal theory for waveguides with anisotropic surface impedance boundaries," *IEEE Transactions on Microwave Theory and Techniques*, vol. 64, no. 4, pp. 1153–1162, 2016.

[52] B. Byrne, "Etude et conception de guides d'onde et d'antennes cornets à métamatériaux," Ph.D. dissertation, 2016.

[53] M. N. Legenkiy and A. Y. Butrym, "Method of mode matching in time domain," *Progress In Electromagnetics Research*, vol. 22, pp. 257–283, 2010.

[54] B. Byrne, N. Capet, and N. Raveu, "Dispersion properties of corrugated waveguides based on the modal theory," in *Proc. 8th Eur. Conf. Antennas Propag.*, 2014, pp. 1–3.

[55] B. Byrne, N. Raveu, N. Capet, G. Le Fur, and L. Duchesne, "Reduction of rectangular waveguide cross-section with metamaterials: A new approach," in *Advanced Electromagnetic Materials in Microwaves and Optics (METAMATERIALS), 2015 9th International Congress on.* IEEE, 2015, pp. 40–42.

[56] ——, "Modal analysis of rectangular waveguides with 2d metamaterials," *Progress In Electromagnetics Research*, vol. 70, pp. 165–173, 2016.

[57] L. Kuhler, G. Le Fur, L. Duchesne, and N. Raveu, "The propagation characteristics of 2-d metamaterial waveguides using the modal expansion theory," *IEEE Transactions on Microwave Theory and Techniques*, no. 99, pp. 1–8, 2018.

[58] B. Byrne, N. Raveu, N. Capet, G. L. Fur, and L. Duchesne, "Field distribution of rectangular waveguides with anisotropic walls by using the modal theory," in *2016 IEEE International Symposium on Antennas and Propagation (APSURSI)*, June 2016, pp. 1091–1092.

[59] N. Engheta and R. W. Ziolkowski, *Metamaterials: physics and engineering explorations.* John Wiley & Sons, 2006.

[60] C. C. S. Technology, https://www.cst.com.

[61] Y. Zhu, "Modeling of high impedance surface structures," Ph.D. dissertation, Université Paris Sud-Paris XI, 2011.

[62] S. Ramo, J. R. Whinnery, and T. Van Duzer, *Fields and waves in communication electronics.* John Wiley & Sons, 2008.

[63] H. Li, F.-F. Li, D.-G. Fan, F.-G. Meng, and R.-X. Wu, "Wideband electromagnetic absorber based on array of parallel-plate waveguide," in *Electromagnetics in Advanced Applications (ICEAA), 2017 International Conference on.* IEEE, 2017, pp. 1224–1226.

[64] F. Costa, A. Monorchio, and G. Manara, "Analysis and design of ultra thin electromagnetic absorbers comprising resistively loaded high impedance surfaces," *IEEE Transactions on Antennas and Propagation*, vol. 58, no. 5, pp. 1551–1558, 2010.

[65] A. Vallecchi, J. R. De Luis, F. Capolino, and F. De Flaviis, "Low profile fully planar folded dipole antenna on a high impedance surface," *IEEE Transactions on Antennas and Propagation*, vol. 60, no. 1, pp. 51–62, 2012.

[66] M. Li, S.-Q. Xiao, and B.-Z. Wang, "Investigation of using high impedance surfaces for wide-angle scanning arrays," *IEEE Transactions on Antennas and Propagation*, vol. 63, no. 7, pp. 2895–2901, 2015.

[67] R. Guzmán-Quirós, J. L. Gomez-Tornero, A. R. Weily, and Y. J. Guo, "Electronically steerable 1-d fabry-perot leaky-wave antenna employing a tunable high impedance surface," *IEEE Transactions on Antennas and Propagation*, vol. 60, no. 11, pp. 5046–5055, 2012.

[68] X.-C. Wang, W.-S. Zhao, J. Hu, and W.-Y. Yin, "Reconfigurable terahertz leaky-wave antenna using graphene-based high-impedance surface," *IEEE Transactions on Nanotechnology*, vol. 14, no. 1, pp. 62–69, 2015.

[69] S. Shahparnia and O. M. Ramahi, "Electromagnetic interference (emi) reduction from printed circuit boards (pcb) using electromagnetic bandgap structures," *IEEE Transactions on Electromagnetic Compatibility*, vol. 46, no. 4, pp. 580–587, 2004.

[70] T. Kamgaing and O. M. Ramahi, "A novel power plane with integrated simultaneous switching noise mitigation capability using high impedance surface," *IEEE Microwave and wireless components letters*, vol. 13, no. 1, pp. 21–23, 2003.

[71] A. Ludwig, C. D. Sarris, and G. V. Eleftheriades, "Metascreen-based superdirective antenna in the optical frequency regime," *Physical review letters*, vol. 109, no. 22, p. 223901, 2012.

[72] D. Sievenpiper, L. Zhang, R. F. Broas, N. G. Alexopolous, and E. Yablonovitch, "High-impedance electromagnetic surfaces with a forbidden frequency band," *IEEE Transactions on Microwave Theory and techniques*, vol. 47, no. 11, pp. 2059–2074, 1999.

[73] M. Hosseinipanah and Q. Wu, "Miniaturised high-impedance surface with high angular stability of resonant frequency," *Electronics letters*, vol. 45, no. 24, pp. 1204–1206, 2009.

[74] H. Sagan, *Space-filling curves.* Springer Science & Business Media, 2012.

[75] J. McVay, N. Engheta, and A. Hoorfar, "High impedance metamaterial surfaces using hilbert-curve inclusions," *IEEE Microwave and Wireless components letters*, vol. 14, no. 3, pp. 130–132, 2004.

[76] D. J. Kern, D. H. Werner, A. Monorchio, L. Lanuzza, and M. J. Wilhelm, "The design synthesis of multiband artificial magnetic conductors using high impedance frequency selective surfaces," *IEEE Transactions on Antennas and Propagation*, vol. 53, no. 1, pp. 8–17, 2005.

[77] O. Luukkonen, A. Yakovlev, C. Simovski, and S. Tretyakov, "Comparative study of surface waves on high-impedance surfaces with and without vias," in *Antennas and Propagation Society International Symposium, 2008. AP-S 2008. IEEE.* IEEE, 2008, pp. 1–4.

[78] O. Luukkonen, C. Simovski, G. Granet, G. Goussetis, D. Lioubtchenko, A. V. Raisanen, and S. A. Tretyakov, "Simple and accurate analytical model of planar grids and high-impedance surfaces comprising metal strips or patches," *IEEE Transactions on Antennas and Propagation*, vol. 56, no. 6, pp. 1624–1632, 2008.

[79] J. P. Gianvittorio, J. Romeu, S. Blanch, and Y. Rahmat-Samii, "Self-similar prefractal frequency selective surfaces for multiband and dual-polarized applications," *IEEE Transactions on Antennas and Propagation*, vol. 51, no. 11, pp. 3088–3096, 2003.

[80] F. Yang and Y. Rahmat-Samii, *Electromagnetic band gap structures in antenna engineering*. Cambridge university press Cambridge, UK, 2009.

[81] K. S. Kunz and R. J. Luebbers, *The finite difference time domain method for electromagnetics*. CRC press, 1993.

[82] J. S. Bagby, D. Nyquist, and B. Drachman, "Integral formulation for analysis of integrated dielectric waveguides," *IEEE transactions on microwave theory and techniques*, vol. 33, no. 10, pp. 906–915, 1985.

[83] M. Koshiba and M. Suzuki, "Application of the boundary-element method to waveguide discontinuities (short paper)," *IEEE transactions on microwave theory and techniques*, vol. 34, no. 2, pp. 301–307, 1986.

[84] M. Hosseinipanah and Q. Wu, "Polarization-dependent artificial magnetic conductor structures using asymmetrical frequency selective surface," in *Microwave, Antenna, Propagation and EMC Technologies for Wireless Communications, 2009 3rd IEEE International Symposium on.* IEEE, 2009, pp. 707–710.

[85] D. M. Pozar, *Microwave engineering.* John Wiley & Sons, 2012.

[86] ANSYS, https://www.ansys.com.

A Development of the analytic equations of section 3

A.1 Definition of hybrid modes:

$$E_z = (\alpha_- e^{jk_x x} + \alpha_+ e^{-jk_x x}) \sin(k_y y) \tag{A.1}$$

$$H_z = (\delta_- e^{jk_x x} + \delta_+ e^{-jk_x x}) \cos(k_y y) \tag{A.2}$$

Where k_x is not determined and $k_y = m\pi/b$

A.2 Transversal fields definitions

$$E_x = -j[\gamma_z k_x(\alpha_- e^{jk_x x} - \alpha_+ e^{-jk_x x}) - Z_0 k_0 k_y(\delta_- e^{jk_x x} + \delta_+ e^{-jk_x x})] \frac{\sin(k_y y)}{k_c^2} \tag{A.3}$$

$$E_y = -[\gamma_z k_y(\alpha_- e^{jk_x x} + \alpha_+ e^{-jk_x x}) + Z_0 k_0 k_x(\delta_- e^{jk_x x} - \delta_+ e^{-jk_x x})] \frac{\cos(k_y y)}{k_c^2} \tag{A.4}$$

$$H_x = -j[-k_0 k_y(\alpha_- e^{jk_x x} + \alpha_+ e^{-jk_x x}) + Z_0 \gamma_z k_x(\delta_- e^{jk_x x} - \delta_+ e^{-jk_x x})] \frac{\cos(k_y y)}{Z_0 k_c^2} \tag{A.5}$$

$$H_y = [k_0 k_x(\alpha_- e^{jk_x x} - \alpha_+ e^{-jk_x x}) + Z_0 \gamma_z k_x(\delta_- e^{jk_x x} + \delta_+ e^{-jk_x x})] \frac{\sin(k_y y)}{Z_0 k_c^2} \tag{A.6}$$

A.3 Boundary conditions

$$Z_{t1} = \left.\frac{E_y}{H_z}\right|_{x=-a} \tag{A.7}$$

$$Z_{z1} = -\left.\frac{E_z}{H_y}\right|_{x=-a} \tag{A.8}$$

$$Z_{t2} = -\left.\frac{E_y}{H_z}\right|_{x=a} \tag{A.9}$$

$$Z_{z2} = \left.\frac{E_z}{H_y}\right|_{x=a} \tag{A.10}$$

By replacing the field equations (A.1), (A.2) and (A.3) to (A.6) on the new boundary conditions (A.7) to (A.10), we get following matrix form:

$$[M]\,(\alpha_-,\alpha_+,\delta_-,\delta_+) = \overrightarrow{0} \tag{A.11}$$

Where:

$$[M] = \begin{bmatrix} uX & u & (f+e_1)X & e_1-f \\ u & uX & -e_2+f & -(e_2+f)X \\ (g_1+h)X & -g_1+h & v_1X & v_1 \\ g_2-h & -(g_2+h)X & v_2 & v_2X \end{bmatrix} \tag{A.12}$$

Where $u = \gamma k_y$, $f = Z_0 k_0 k_x$, $e_1 = Z_{t1} k_c^2$, $e_2 = Z_{t2} k_c^2$, $h = Z_0 k_c^2$, $g_1 = Z_{z1} k_0 k_x$, $g_2 = Z_{z2} k_0 k_x$, $v_1 = Z_{z1} Z_0 \gamma k_y$, $v_2 = Z_{z2} Z_0 \gamma k_y$ and $X = e^{-2jk_x a}$.

A.4   Case m=0

If we consider the case where $m = 0$, this will imply $k_y = m\pi/b = 0$ and also $E_z = 0$, hence the transversal electromagnetic fields are as follows:

$$E_x = 0 \tag{A.13}$$

$$E_y = -\frac{Z_0 k_0 k_x (\delta_- e^{jk_x x} - \delta_+ e^{-jk_x x})}{k_c^2} \tag{A.14}$$

$$H_x = -\frac{j\gamma k_x (\delta_- e^{jk_x x} - \delta_+ e^{-jk_x x})}{k_c^2} \tag{A.15}$$

$$H_y = 0 \tag{A.16}$$

The dispersion equation will be independent of Z_{z1} and Z_{z2}, hence, evaluating the fields on the boundaries (A.7) and (A.9) results in:

$$Z_{t1} = \left.\frac{E_y}{H_z}\right|_{x=-a}$$

$$(Z_0 k_x k_0 + Z_{t1} k_c^2) e^{-jk_x a}\delta_- + (-Z_0 k_x k_0 + Z_{t1} k_c^2) e^{jk_x a}\delta_+ \tag{A.17}$$

$$Z_{t2} = -\left.\frac{E_y}{H_z}\right|_{x=a}$$

$$(-Z_0 k_x k_0 + Z_{t2} k_c^2) e^{jk_x a}\delta_- + (Z_0 k_x k_0 + Z_{t2} k_c^2) e^{-jk_x a}\delta_+ \tag{A.18}$$

Reorganizing (A.17) and (A.18) in matrix form:

$$\begin{bmatrix} \left(Z_0 k_x k_0 + Z_{t1} k_c^2\right) e^{-jk_x a} & \left(-Z_0 k_x k_0 + Z_{t1} k_c^2\right) e^{jk_x a} \\ \left(-Z_0 k_x k_0 + Z_{t2} k_c^2\right) e^{jk_x a} & \left(Z_0 k_x k_0 + Z_{t2} k_c^2\right) e^{-jk_x a} \end{bmatrix} \begin{bmatrix} \delta_- \\ \delta_+ \end{bmatrix} = 0 \tag{A.19}$$

Calculating det(M) of (A.19):

$$\left(Z_0 k_x k_0 + Z_{t1} k_c^2\right)\left(Z_0 k_x k_0 + Z_{t2} k_c^2\right) e^{-2jk_x a} +$$

$$-\left(-Z_0 k_x k_0 + Z_{t1} k_c^2\right)\left(-Z_0 k_x k_0 + Z_{t2} k_c^2\right) e^{2jk_x a} = 0$$

$$\tan(2k_x a) = -\frac{j Z_0 k_x k_0 k_c^2 (Z_{t1} + Z_{t2})}{k_c^4 (Z_{t1} Z_{t2}) + (Z_0 k_x k_0)^2} \tag{A.20}$$

Replacing (A.20) with $k_c = \sqrt{k_x^2 + k_y^2}$:

$$\tan(2k_x a) = -\frac{j Z_0 k_x k_0 \left(k_x^2 + k_y^2\right)(Z_{t1} + Z_{t2})}{\left(k_x^2 + k_y^2\right)^2 (Z_{t1} Z_{t2}) + (Z_0 k_x k_0)^2}$$

$$\tan(2k_x a) = -\frac{j Z_0 k_x k_0 (Z_{t1} + Z_{t2})}{\left(k_x^2 + k_y^2\right)\left((Z_{t1} Z_{t2}) + \frac{(Z_0 k_x k_0)^2}{\left(k_x^2 + k_y^2\right)^2}\right)} \tag{A.21}$$

Which is valid a solution and must be solved numerically.

A.5   Case $Z_{z1}, Z_{z2} = 0$

$$Z_{t1} = \left.\frac{E_y}{H_z}\right|_{x=-a}$$

$$\gamma_z k_y e^{-j k_x a} \alpha_- + \left(Z_0 k_0 k_x + Z_{t1} k_c^2\right) e^{-j k_x a} \delta_- +$$

$$+ \gamma_z k_y e^{j k_x a} \alpha_+ + \left(-Z_0 k_0 k_x + Z_{t1} k_c^2\right) e^{j k_x a} \delta_+ = 0 \quad \text{(A.22)}$$

$$Z_{t2} = -\left.\frac{E_y}{H_z}\right|_{x=a}$$

$$-\gamma_z k_y e^{j k_x a} \alpha_- + \left(-Z_0 k_0 k_x + Z_{t2} k_c^2\right) e^{j k_x a} \delta_- +$$

$$-\gamma_z k_y e^{-j k_x a} \alpha_+ + \left(Z_0 k_0 k_x + Z_{t2} k_c^2\right) e^{-j k_x a} \delta_+ = 0 \quad \text{(A.23)}$$

$$Z_{z1} = 0 = -\frac{E_z}{H_y}\bigg|_{x=-a}$$

$$e^{-jk_x a}\alpha_- + e^{jk_x a}\alpha_+ = 0 \tag{A.24}$$

$$Z_{z2} = 0 = \frac{E_z}{H_y}\bigg|_{x=a}$$

$$-e^{jk_x a}\alpha_- - e^{-jk_x a}\alpha_+ = 0 \tag{A.25}$$

From (A.24):

$$\alpha_- = -e^{2jk_x a}\alpha_+ \tag{A.26}$$

Introducing (A.26) in (A.25) leads to:

$$\left(e^{3jk_x a} - e^{-jk_x a}\right)\alpha_+ = 0 \tag{A.27}$$

Equation (A.27) leads to two possible solutions:

Solution 1:

$$\alpha_+ = \alpha_- = 0 \tag{A.28}$$

This will yield to the case where m=0 and thus the general matrix reduces to:

$$\begin{bmatrix} \left(Z_0 k_0 k_x + Z_{t1} k_c^2\right)e^{-jk_x a} & \left(-Z_0 k_0 k_x + Z_{t1} k_c^2\right)e^{jk_x a} \\ \left(-Z_0 k_0 k_x + Z_{t2} k_c^2\right)e^{jk_x a} & \left(Z_0 k_0 k_x + Z_{t2} k_c^2\right)e^{-jk_x a} \end{bmatrix}\begin{bmatrix} \delta_- \\ \delta_+ \end{bmatrix} = \begin{bmatrix} 0 \\ 0 \end{bmatrix} \tag{A.29}$$

Solution 2:

From (A.27):

$$e^{3jk_x a} - e^{-jk_x a} = 0$$

$$e^{jk_x a}\left(e^{2jk_x a} - e^{-2jk_x a}\right) = 0$$

$$e^{jk_x a}\left(2j\sin\left(2k_x a\right)\right) = 0$$

$$k_x = \frac{n\pi}{2a} \tag{A.30}$$

With "n" an Integer, and assuming $a \neq 0$.

Using (A.30) on (A.27):

$$\alpha_- = -e^{jn\pi}\alpha_+$$

$$\alpha_- = -(-1)^n \alpha_+ \tag{A.31}$$

Because $e^{jn\pi} = (-1)^n$, $\forall n \in \mathbb{Z}$. From here we have two cases for "n":

- Case n=2p

  This implies:

$$k_x = \frac{p\pi}{a} \tag{A.32}$$

$$\alpha_- = -\alpha_+ \tag{A.33}$$

  Which, if we use (A.32) and (A.33) on eqs. (A.22) and (A.23) we get:

$$\gamma_z k_y \left(2j\sin\left(p\pi\right)\right)\alpha_+ + \left(Z_0 k_0 \frac{p\pi}{a} + Z_{t1} k_c^2\right)e^{-jp\pi}\delta_- +$$

$$+ \left(-Z_0 k_0 \frac{p\pi}{a} + Z_{t1} k_c^2\right)e^{jp\pi}\delta_+ = 0 \quad \text{(A.34)}$$

$$\gamma_z k_y \left(2j\sin\left(p\pi\right)\right)\alpha_+ + \left(-Z_0 k_0 \frac{p\pi}{a} + Z_{t2} k_c^2\right)e^{jp\pi}\delta_- +$$

$$+ \left(Z_0 k_0 \frac{p\pi}{a} + Z_{t2} k_c^2\right)e^{-jp\pi}\delta_+ = 0 \quad \text{(A.35)}$$

For every value of "p", $\sin(p\pi)$ goes to cero, so eqs (A.34) and (A.35) will be:

$$\left(Z_0 k_0 \frac{p\pi}{a} + Z_{t1} k_c^2\right)e^{-jp\pi}\delta_- + \left(-Z_0 k_0 \frac{p\pi}{a} + Z_{t1} k_c^2\right)e^{jp\pi}\delta_+ = 0$$

$$\left(-Z_0 k_0 \frac{p\pi}{a} + Z_{t2} k_c^2\right)e^{jp\pi}\delta_- + \left(Z_0 k_0 \frac{p\pi}{a} + Z_{t2} k_c^2\right)e^{-jp\pi}\delta_+ = 0$$

Also $e^{jp\pi} = e^{-jp\pi} = (-1)^p$, then:

$$\left(Z_0 k_0 \frac{p\pi}{a} + Z_{t1} k_c^2\right)(-1)^p \delta_- + \left(-Z_0 k_0 \frac{p\pi}{a} + Z_{t1} k_c^2\right)(-1)^p \delta_+ = 0 \tag{A.36}$$

$$\left(-Z_0 k_0 \frac{p\pi}{a} + Z_{t2} k_c^2\right)(-1)^p \delta_- + \left(Z_0 k_0 \frac{p\pi}{a} + Z_{t2} k_c^2\right)(-1)^p \delta_+ = 0 \tag{A.37}$$

Eqs. (A.36) and (A.37) can be reduced by factoring $(-1)^p$, thus:

$$\begin{bmatrix} \left(Z_0 k_0 \frac{p\pi}{a} + Z_{t1} k_c^2\right) & \left(-Z_0 k_0 \frac{p\pi}{a} + Z_{t1} k_c^2\right) \\ \left(-Z_0 k_0 \frac{p\pi}{a} + Z_{t2} k_c^2\right) & \left(Z_0 k_0 \frac{p\pi}{a} + Z_{t2} k_c^2\right) \end{bmatrix} \begin{bmatrix} \delta_- \\ \delta_+ \end{bmatrix} = \vec{0} \tag{A.38}$$

Doing the operation (A.36) + (A.37) we get the following results:

$$(Z_{t1} + Z_{t2})k_c^2 \delta_- + (Z_{t1} + Z_{t2})k_c^2 \delta_+ = 0$$

$$(Z_{t1} + Z_{t2})k_c^2(\delta_- + \delta_+) = 0 \tag{A.39}$$

Which are not valid because it gives two solutions: $k_c = 0$ or $Z_{t1} = -Z_{t2}$ and $\delta_- = -\delta_+$.

- Case n=(2p+1)

  This implies:

$$k_x = \frac{(2p+1)\pi}{2a} \tag{A.40}$$

$$\alpha_- = \alpha_+ \tag{A.41}$$

Which, if we use (A.40) and (A.41) on eqs. (A.22) and (A.23):

$$\gamma_z k_y \left(2\cos\left(\frac{(2p+1)\pi}{2}\right)\right)\alpha_+ + \left(Z_0 k_0 \frac{(2p+1)\pi}{2a} + Z_{t1} k_c^2\right)e^{-j\frac{(2p+1)\pi}{2}}\delta_- +$$

$$+ \left(-Z_0 k_0 \frac{(2p+1)\pi}{2a} + Z_{t1} k_c^2\right)e^{j\frac{(2p+1)\pi}{2}}\delta_+ = 0 \quad \text{(A.42)}$$

$$-\gamma_z k_y \left(2\cos\left(\frac{(2p+1)\pi}{2}\right)\right)\alpha_+ + \left(-Z_0 k_0 \frac{(2p+1)\pi}{2a} + Z_{t2} k_c^2\right)e^{j\frac{(2p+1)\pi}{2}}\delta_- +$$

$$+ \left(Z_0 k_0 \frac{(2p+1)\pi}{2a} + Z_{t2} k_c^2\right)e^{-j\frac{(2p+1)\pi}{2}}\delta_+ = 0 \quad \text{(A.43)}$$

For every value of "p", $\cos\left(\frac{(2p+1)\pi}{2}\right)$ goes to zero, thus eqs. (A.42) and (A.43):

$$\left(\frac{Z_0 k_0 (2p+1)\pi}{2a} + Z_{t1} k_c^2\right) e^{-j\frac{(2p+1)\pi}{2}} \delta_- +$$

$$+ \left(-\frac{Z_0 k_0 (2p+1)\pi}{2a} + Z_{t1} k_c^2\right) e^{j\frac{(2p+1)\pi}{2}} \delta_+ = 0 \quad \text{(A.44)}$$

$$\left(-\frac{Z_0 k_0 (2p+1)\pi}{2a} + Z_{t2} k_c^2\right) e^{j\frac{(2p+1)\pi}{2}} \delta_- +$$

$$+ \left(\frac{Z_0 k_0 (2p+1)\pi}{2a} + Z_{t2} k_c^2\right) e^{-j\frac{(2p+1)\pi}{2}} \delta_+ = 0 \quad \text{(A.45)}$$

Also $e^{j\frac{(2p+1)\pi}{2}} = j(-1)^p$ and $e^{-j\frac{(2p+1)\pi}{2}} = -j(-1)^p$, then eqs. (A.44) and (A.45):

$$-\left(\frac{Z_0 k_0 (2p+1)\pi}{2a} + Z_{t1} k_c^2\right)(-1)^p \delta_- +$$

$$+ \left(-\frac{Z_0 k_0 (2p+1)\pi}{2a} + Z_{t1} k_c^2\right)(-1)^p \delta_+ = 0 \quad \text{(A.46)}$$

$$\left(-\frac{Z_0 k_0 (2p+1)\pi}{2a} + Z_{t2} k_c^2\right)(-1)^p \delta_- +$$

$$-\left(\frac{Z_0 k_0 (2p+1)\pi}{2a} + Z_{t2} k_c^2\right)(-1)^p \delta_+ = 0 \quad \text{(A.47)}$$

Eqs (A.46) and (A.47) can be reduced by factoring $(-1)^p$, thus:

$$\begin{bmatrix} -\left(Z_0 k_0 \frac{(2p+1)\pi}{2a} + Z_{t1} k_c^2\right) & \left(-Z_0 k_0 \frac{(2p+1)\pi}{2a} + Z_{t1} k_c^2\right) \\ \left(-Z_0 k_0 \frac{(2p+1)\pi}{2a} + Z_{t2} k_c^2\right) & -\left(Z_0 k_0 \frac{(2p+1)\pi}{a} + Z_{t2} k_c^2\right) \end{bmatrix} \begin{bmatrix} \delta_- \\ \delta_+ \end{bmatrix} = \vec{0} \quad \text{(A.48)}$$

Calculating $\det(M) = 0$ of (A.48) gives:

$$\left(\frac{Z_0 k_0 (2p+1)\pi}{2a} + Z_{t1} k_c^2\right)\left(\frac{Z_0 k_0 (2p+1)\pi}{2a} + Z_{t2} k_c^2\right)$$

$$-\left(-\frac{Z_0 k_0 (2p+1)\pi}{2a} + Z_{t2} k_c^2\right)\left(-\frac{Z_0 k_0 (2p+1)\pi}{2a} + Z_{t1} k_c^2\right) = 0$$

$$k_c^2 (Z_{t1} + Z_{t2})\left(\frac{Z_0 k_0 (2p+1)\pi}{2a}\right) = 0 \tag{A.49}$$

From (A.49), is possible to conclude that is not possible for it to be zero because, $Z_{t1}, Z_{t2} \neq 0$, and $k_c^2 = k_x^2 + k_y^2 \neq 0$.

Thus, the only real solution for the case $Z_{z1}, Z_{z2} = 0$ is solution 1.

B Unit Cell Tutorial for HFSS

1. The "Master1" plane is defined: Right click -> Assign Boundaries -> Master
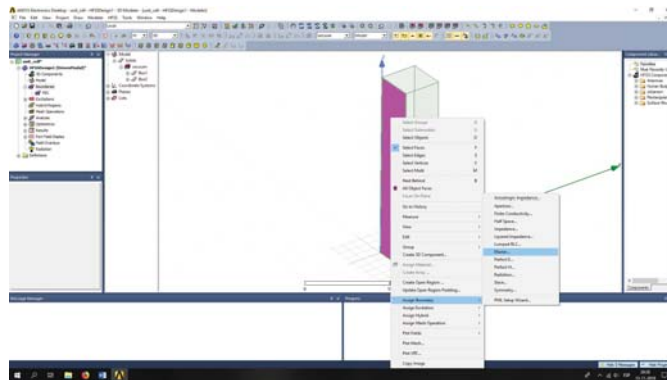
Figure B.1: Assigning the Master plane (1).

2. The vector U of the "Master1" plane is defined, the red arrow shows from and to where the vector is considered.
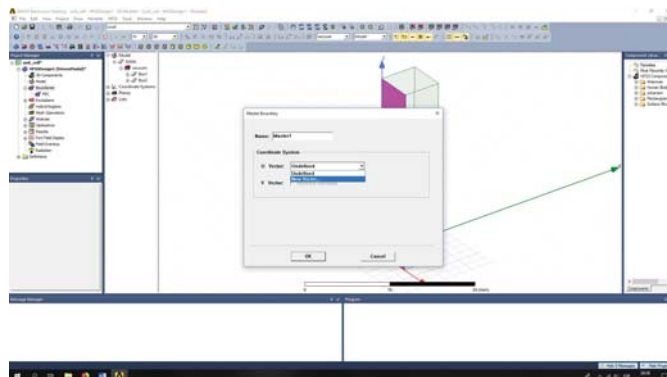
Figure B.2: Assigning the Master plane (2).

3. The vector V must be in the volume, so the box "Reverse direction" should be selected if necessary.
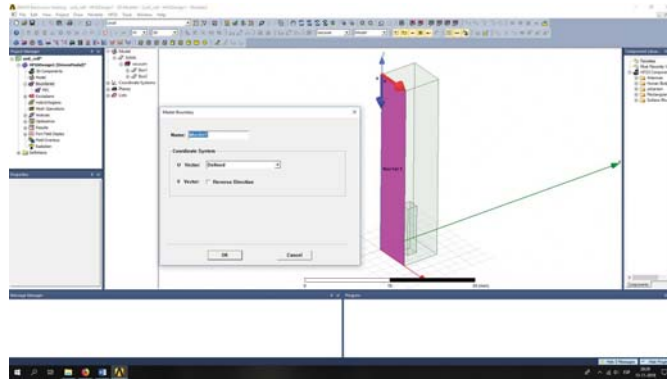
Figure B.3: Assigning the Master plane (3).

4. The result of declaring the "Master1" plane can be seen in the following image:
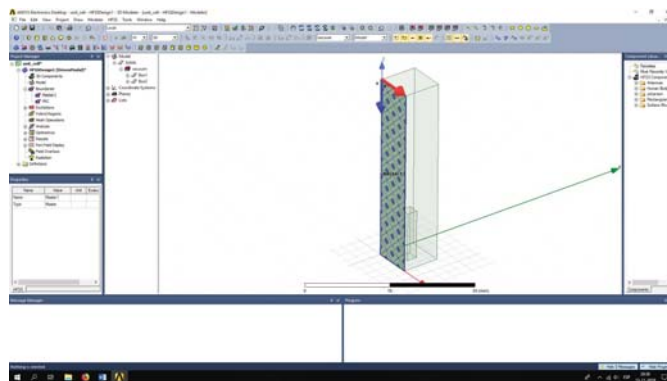
Figure B.4: Assigning the Master plane (4).

5. The "Slave1" plane is defined: Right click -> Assign Boundaries -> Slave
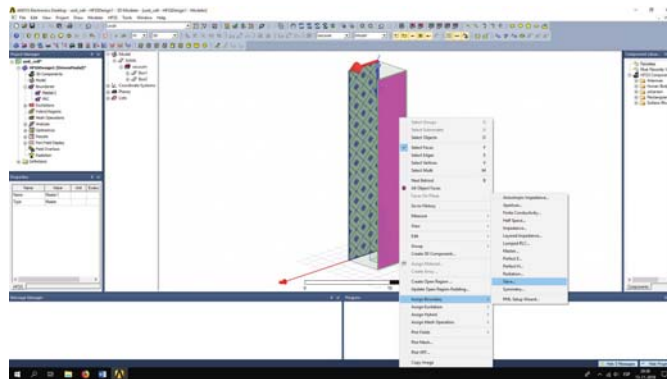
Figure B.5: Assigning the Slave plane (1).

6. In the box "Master Boundary" the option "Master1" is selected. Then we must define the vector U associated with the plane "Slave1" as shown in the following image:
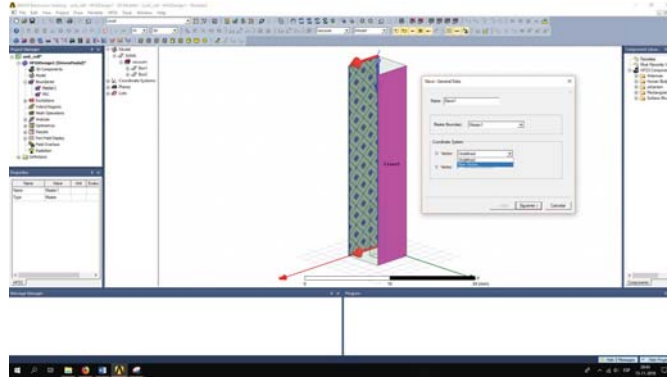
Figure B.6: Assigning the Slave plane (2).

7. Care must be taken to define the vector U (of the "Slave1") in the same direction, parallel and of the same size to the vector U of the "Master1" plane. The result will show a vector in red smaller than the vector of the associated master plane.

8. Similarly, the vector V of "Slave1" must be within the volume, so the "Reverse Direction" box should be selected if necessary.
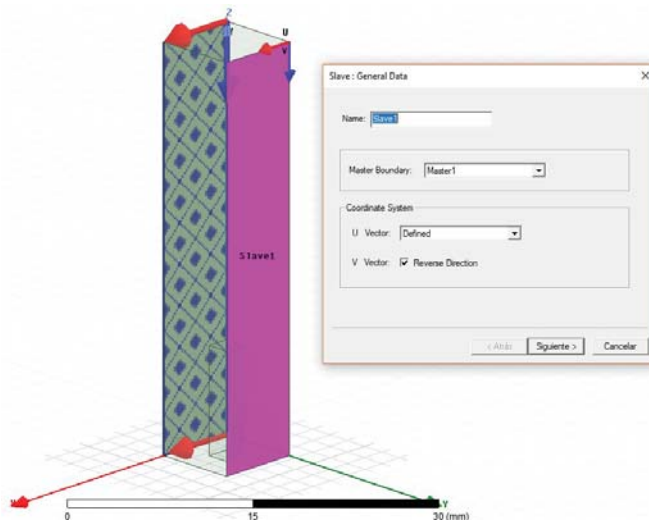
Figure B.7: Assigning the Slave plane (3).

9. To make the scanning angles with the Floquet port, the option "Use scan angles to calculate phase delay" is chosen and the created variables are entered: "phi_scan" and "theta_scan". The angles θ and ϕ considered by HFSS are shown attached to the following image:
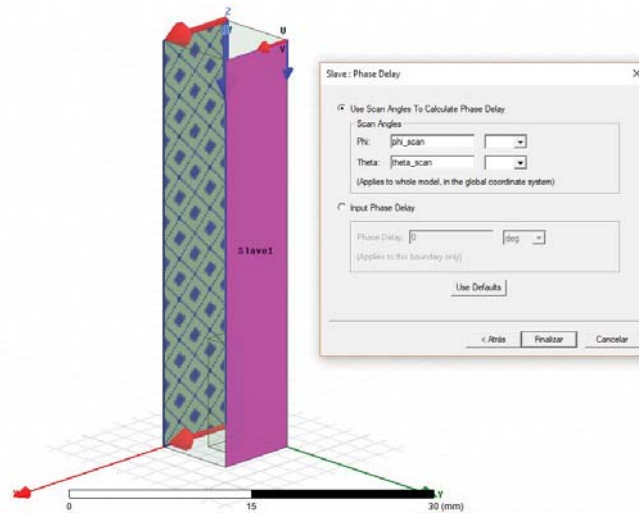
Figure B.8: Defining scanning angles (1).
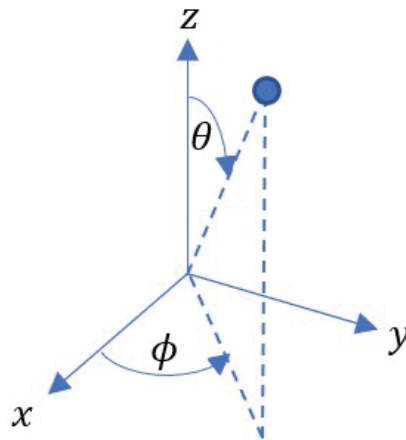
Figure B.9: Defining scanning angles (2).

10. When configuring the "Slave1" plane, the arrow indicating the phase between "Master1" and "Slave1" appears pointing on the same x-axis, this is due to the fact that the variables "phi_scan" and "theta_scan" were defined as 0° and 89° respectively.
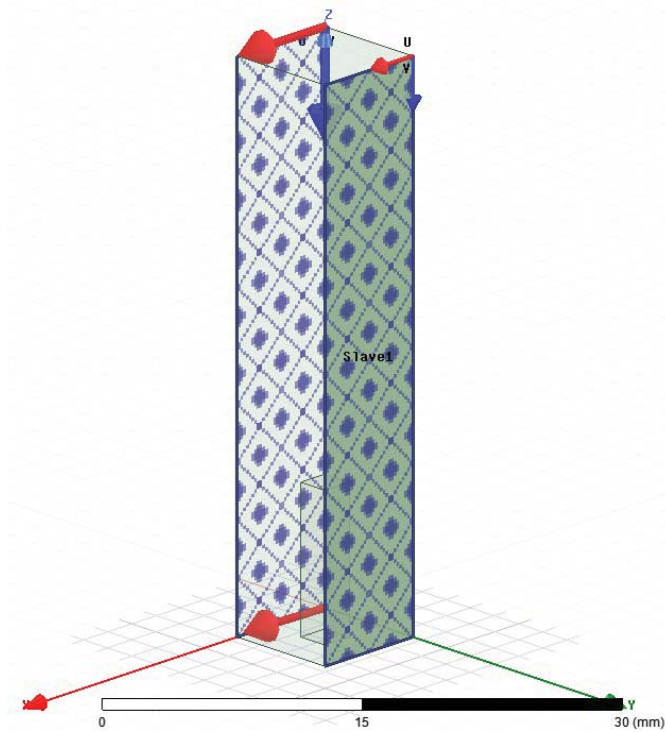
Figure B.10: Defining scanning angles (3).

11. The same steps are repeated to define the plane "Master2" and "Slave2"
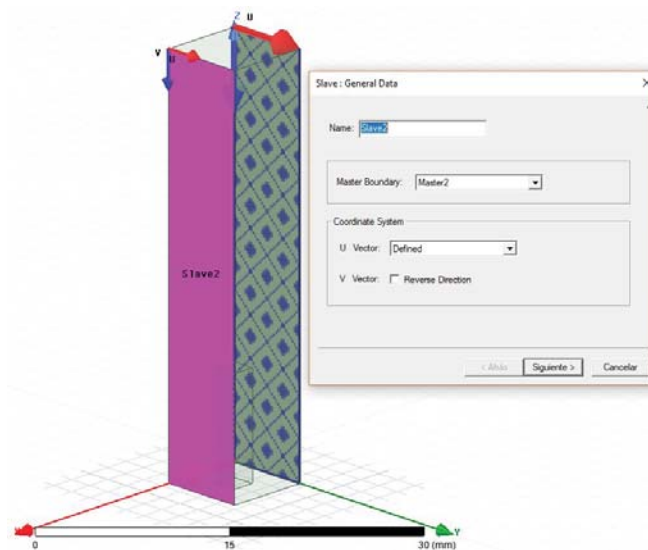
Figure B.11: Master2 and Slave2 definitions (1).

12. When defining the offset in "Slave2" the variables "phi_scan" and "theta_scan" are already in their corresponding boxes, so it only remains to select the "Finish" tab
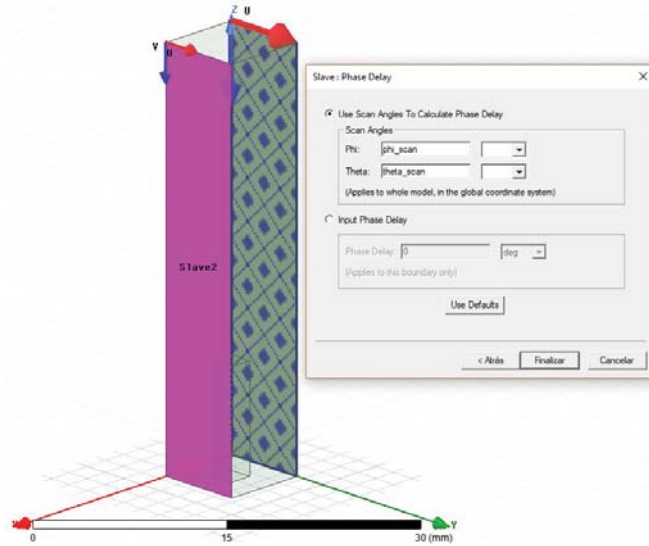
Figure B.12: Master2 and Slave2 definitions (2).

13. To assign floquet ports you must first go to: HFSS -> Solution type -> Modal
14. Then on the upper side: Right click -> Assign Excitation -> Floquet Port
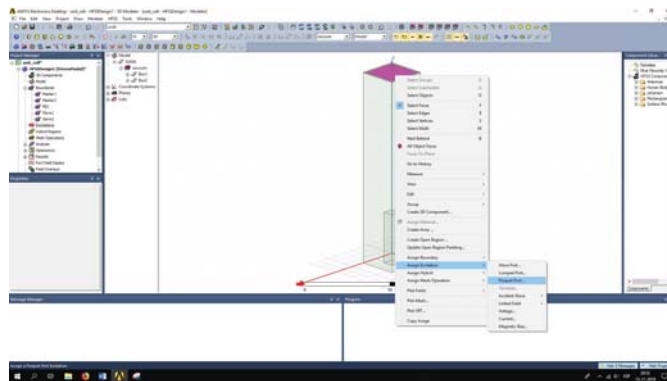
Figure B.13: Assigning Floquet Port (1).

15. The direction of vector A is defined
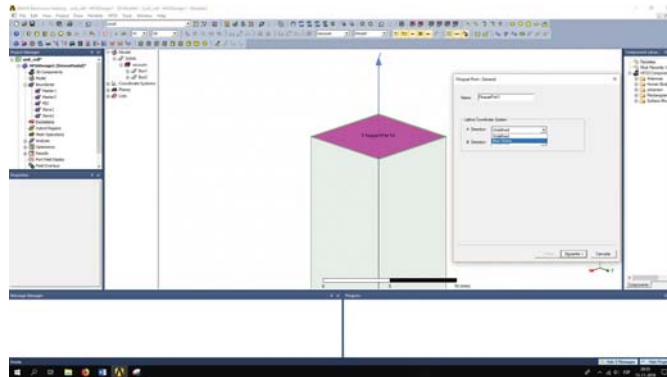
Figure B.14: Assigning Floquet Port (2).

16. Then the address of vector B
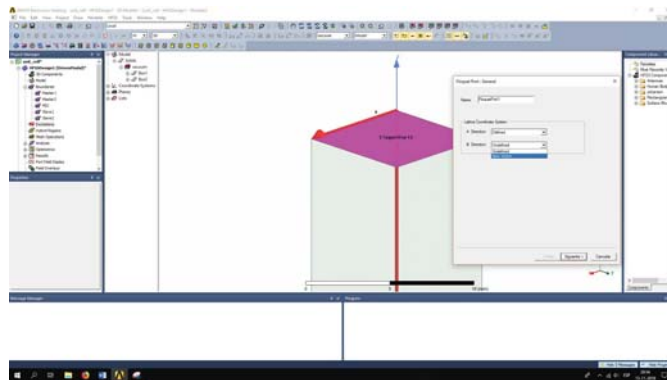
Figure B.15: Assigning Floquet Port (3).

17. The direction of the vectors should look like in the following image:
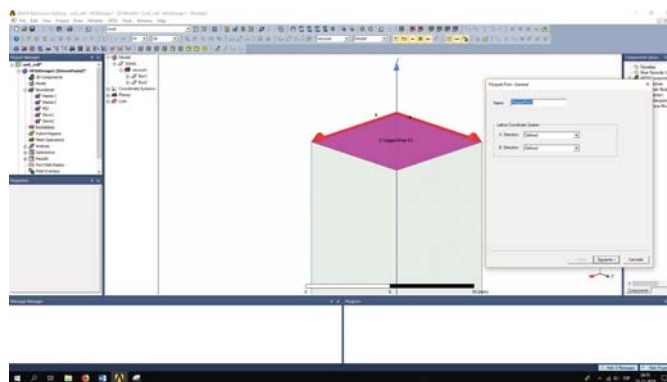
Figure B.16: Assigning Floquet Port (4).

18. The following tab defines the number of modes to be propagated, in our case it is necessary that the TE and TM modes are propagated, so in "Number of modes" it is

placed as 2. Then the "m" and "n" indexes are defined "For mode 1 (TE) and mode 2 (TM), given that the indices" m "and" n "with zero this implies that they are two orthogonal flat waves that propagate with an angle of incidence depending on the variables θ and ϕ (which we previously defined on the faces "Master1" and "Slave1").
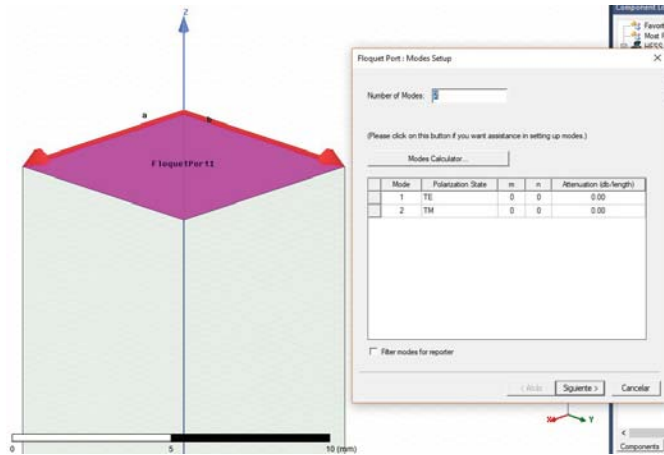
Figure B.17: Assigning Floquet Port (5).

19. Then, since it is necessary to obtain the phase variations at the height of the metama-terial, the "Deembed" option is selected and the height at which the S parameters are calculated, in our case the surface impedance is calculated as: a/2 - h_PIC, where "a" corresponds to the width of the WR284 guide and h_PIC corresponds to the test height used in the [52]
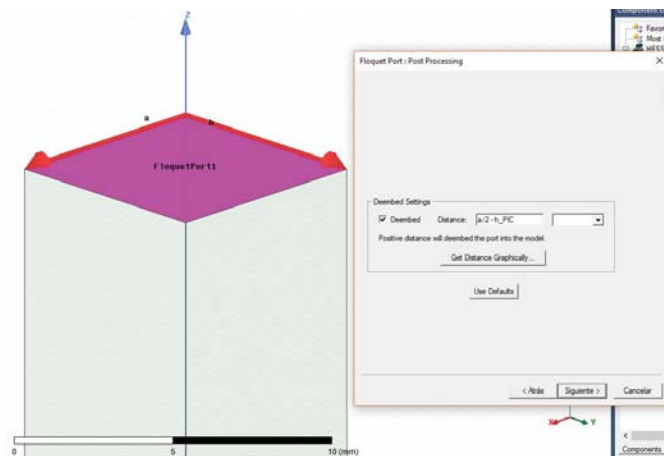
Figure B.18: Assigning Floquet Port - Deembeding (1).

20. The following image shows that floquet modes participate in the generation of adaptive 3D mesh. For more information check the following link in the section Floquet Port: 3D refinement: http://www.1cae.com/articleAccessory/2017/04/16/HFSS%20Floquet%20Ports.pdf
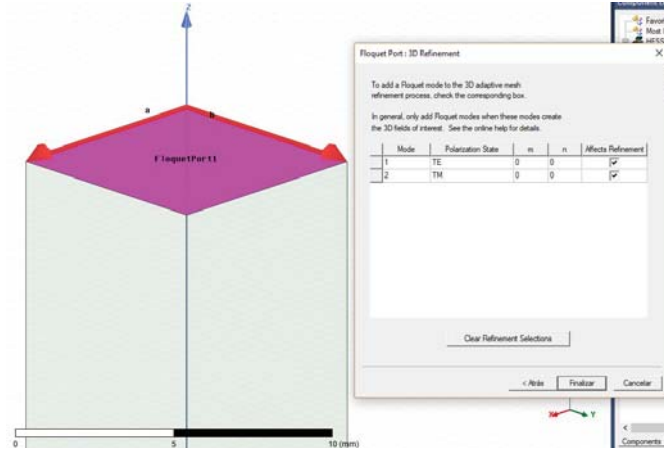
Figure B.19: Assigning Floquet Port - Deembeding (2).

21. The result when you finish configuring the floquet port is seen in the following image, the blue arrow indicates from which height the deembeding is performed.
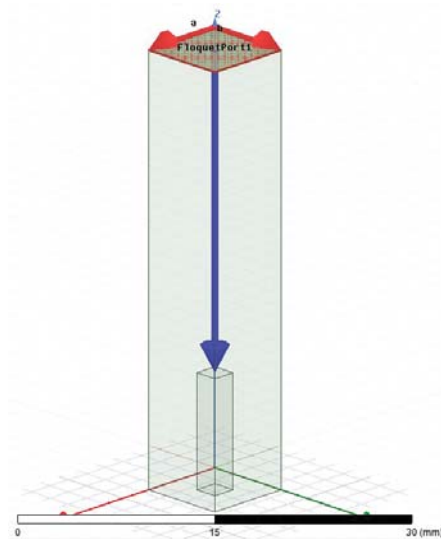
Figure B.20: Assigning Floquet Port - Deembeding (3).

22. The PEC boundary conditions are defined as shown in the following image:
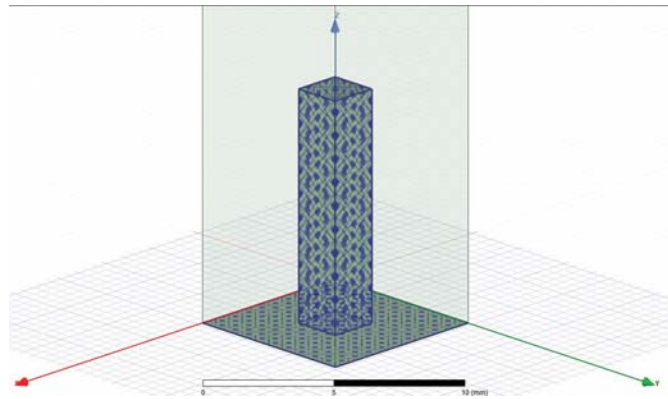
Figure B.21: Assigning PEC boundary conditions.

23. Following the steps in [52] the solution setup is configured.
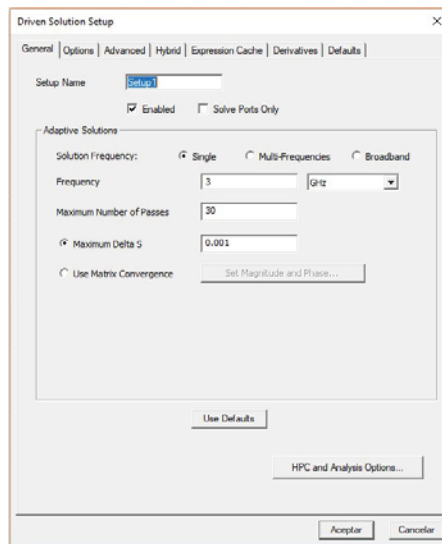
Figure B.22: Configuring Solution setup (1).
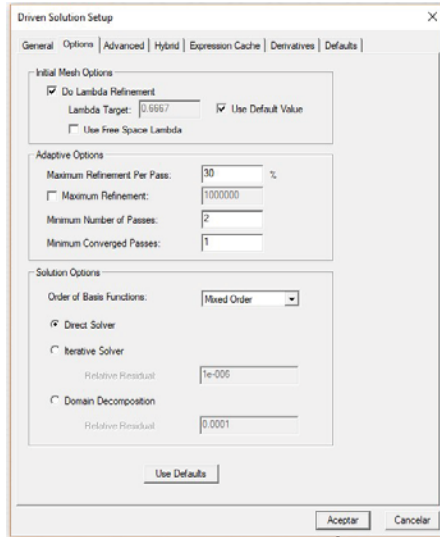
Figure B.23: Configuring Solution setup (2).
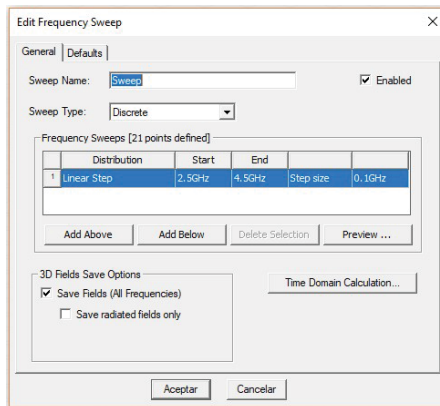
Figure B.24: Configuring Solution setup (3).
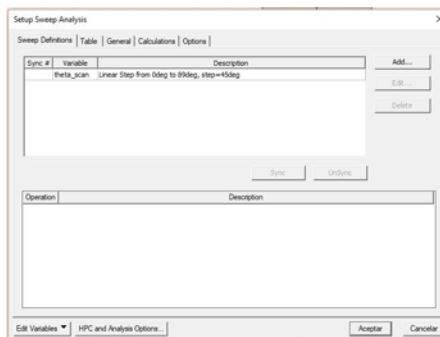
Figure B.25: Configuring Solution setup (4).

24. To create the output variables, go to Project Manager -> Results -> Create Modal Solution Data Report -> Rectangular Plot -> Output Variable. Then, create two output variables
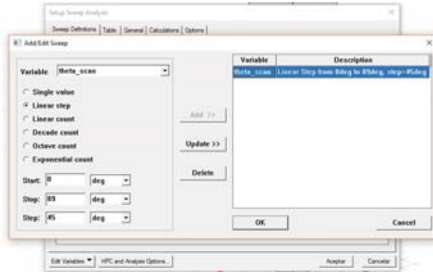
Figure B.26: Configuring Solution setup (5).

Z_z and Z_t, which will be used to obtain the surface impedance according to the following equations:

$$Z_t = \frac{im\left(\dfrac{Z_0}{\cos\left(\dfrac{theta_{scan} \cdot \pi}{180}\right)} \dfrac{1 + S(floquetPort1:1, floquetPort1:1)}{1 - S(floquetPort1:1, floquetPort1:1)}\right)}{Z_0} \quad \text{(B.1)}$$

$$Z_z = \frac{im\left(Z_0 \cdot \cos\left(\dfrac{theta_{scan} \cdot \pi}{180}\right) \dfrac{1 + S(floquetPort1:2, floquetPort1:2)}{1 - S(floquetPort1:2, floquetPort1:2)}\right)}{Z_0}$$

(B.2)

25. These formulas correspond to equations (3.16) and (3.17) of [52]
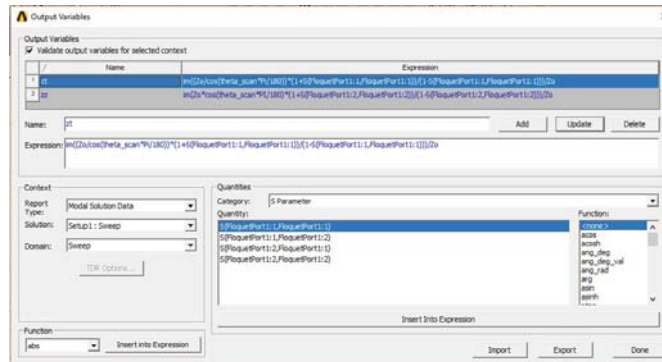
Figure B.27: Defining output variables (1).

26. Finally the variables created are selected in Output Variables
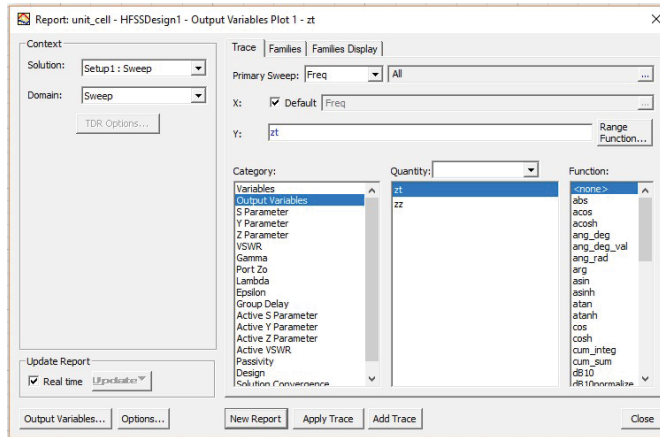
Figure B.28: Defining output variables (2).
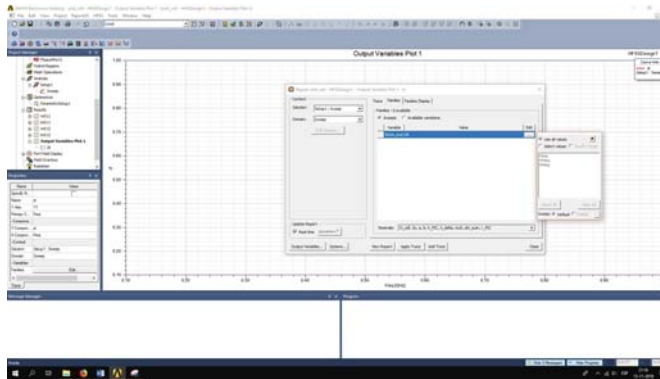
Figure B.29: Defining output variables (3).

C Surface Impedance plots
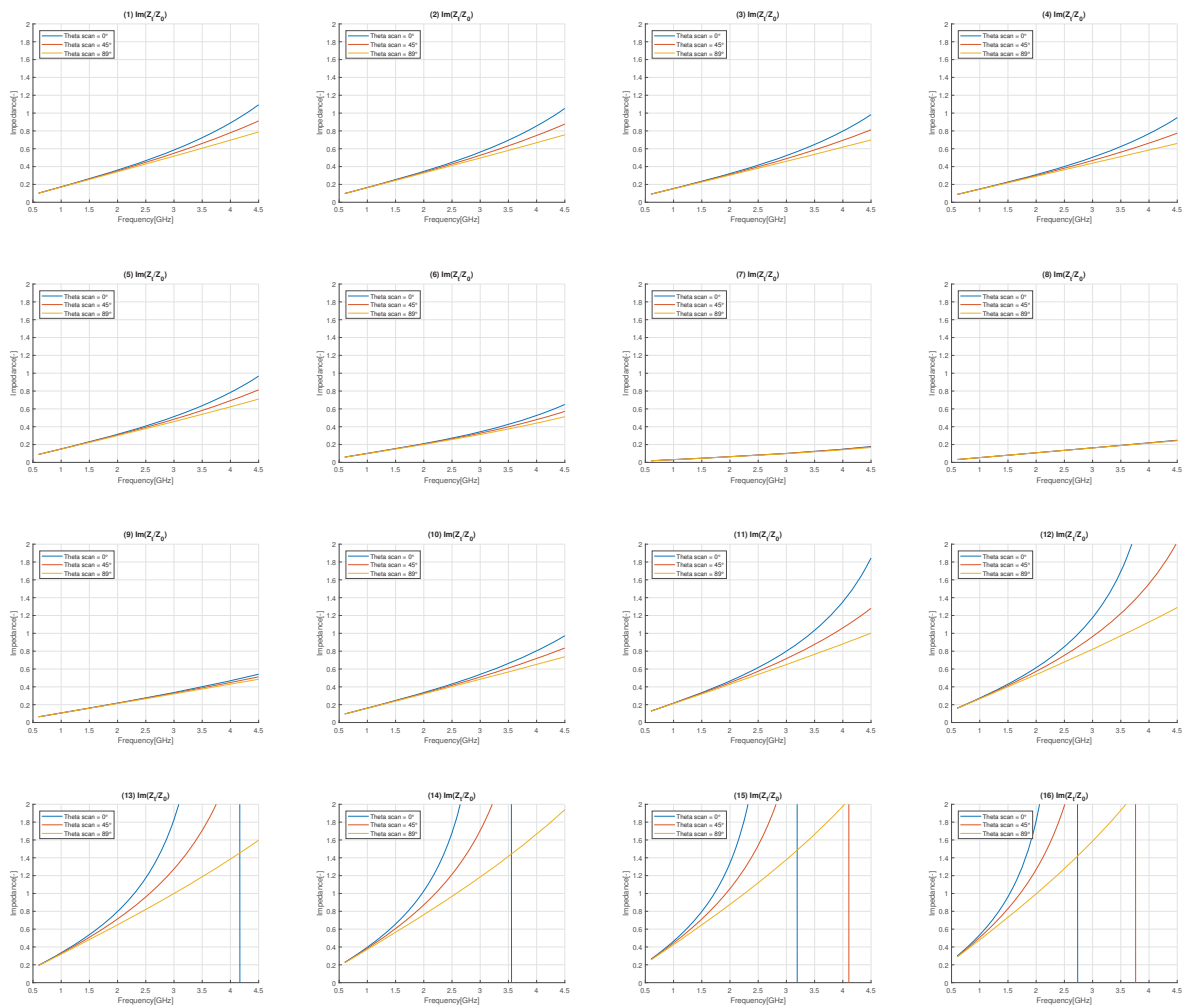
Figure C.1: Z_t iterations, PIC unit cell
.
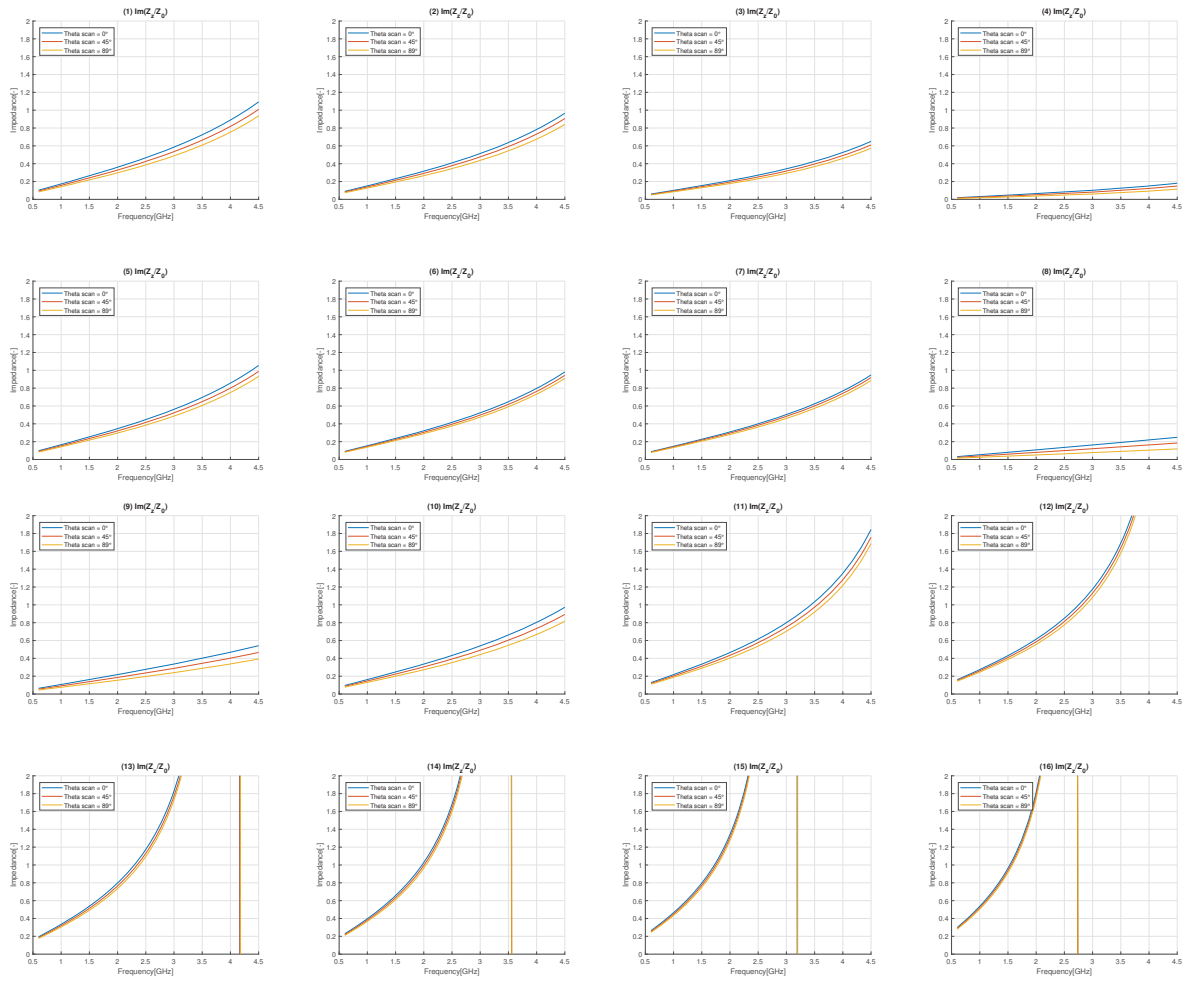
Figure C.2: Z_z iterations, PIC unit cell

.
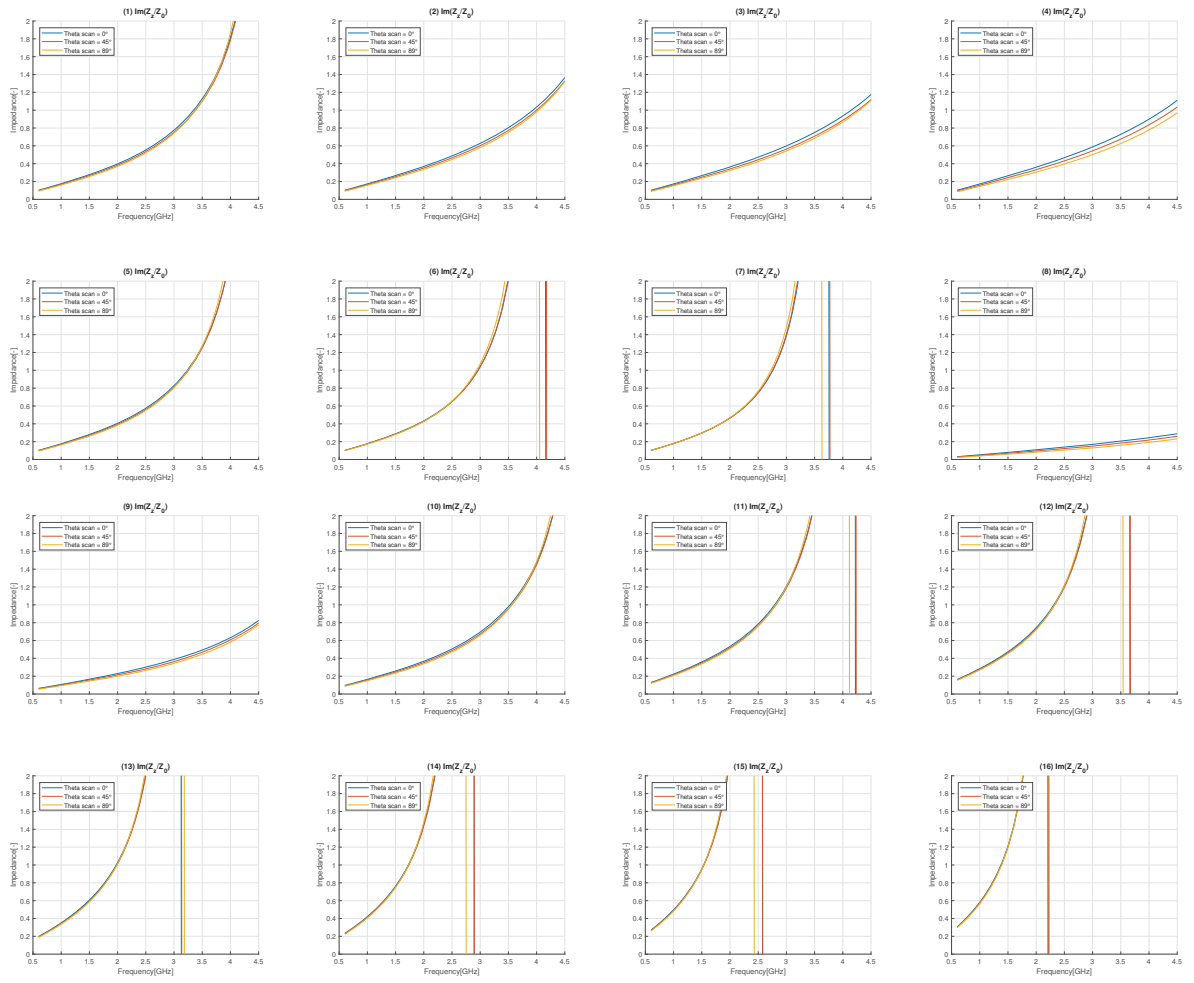
Figure C.3: Z_z iterations, T unit cell (x-axis)

.
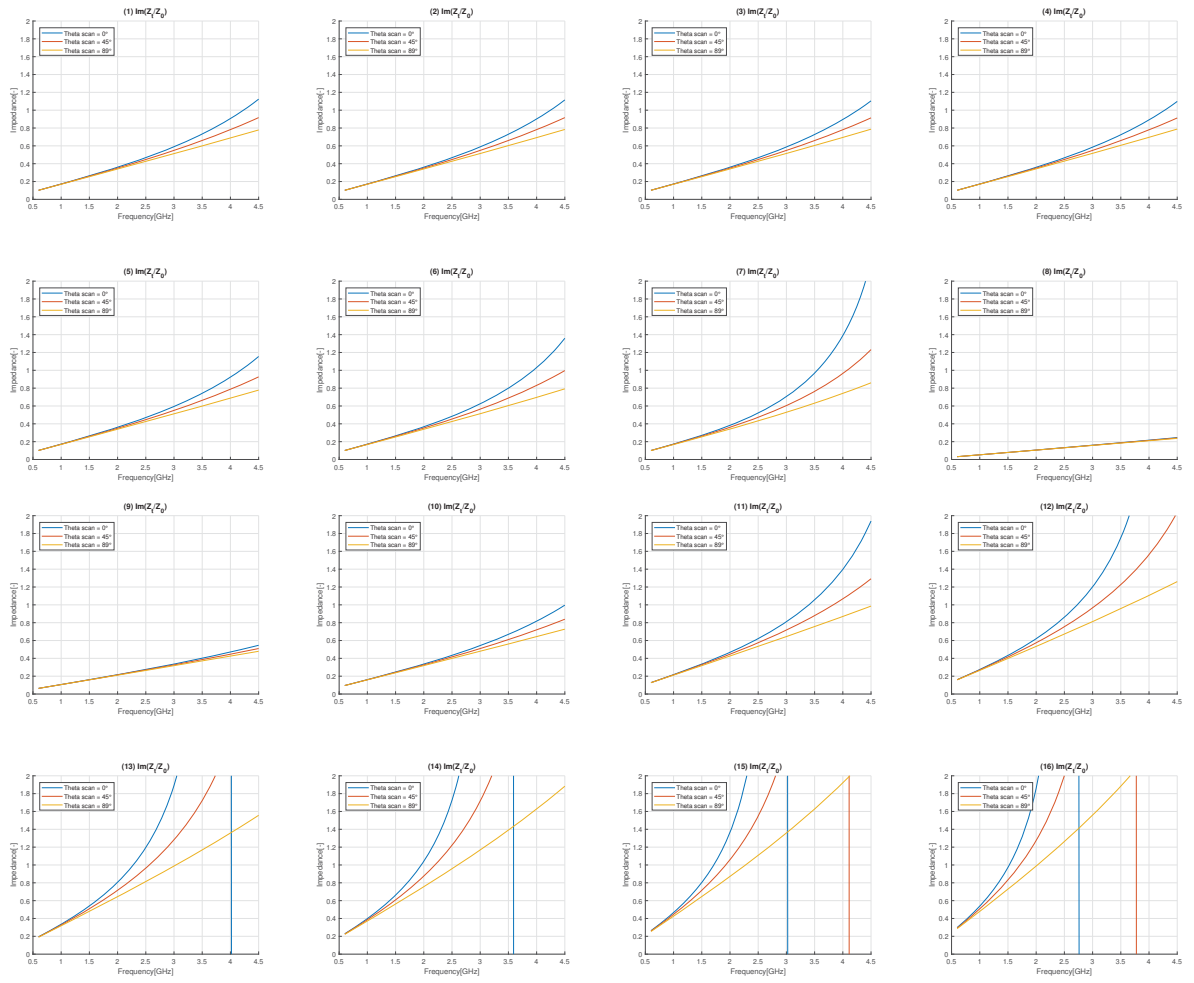
Figure C.4: Z_t iterations, T unit cell (x-axis)

.
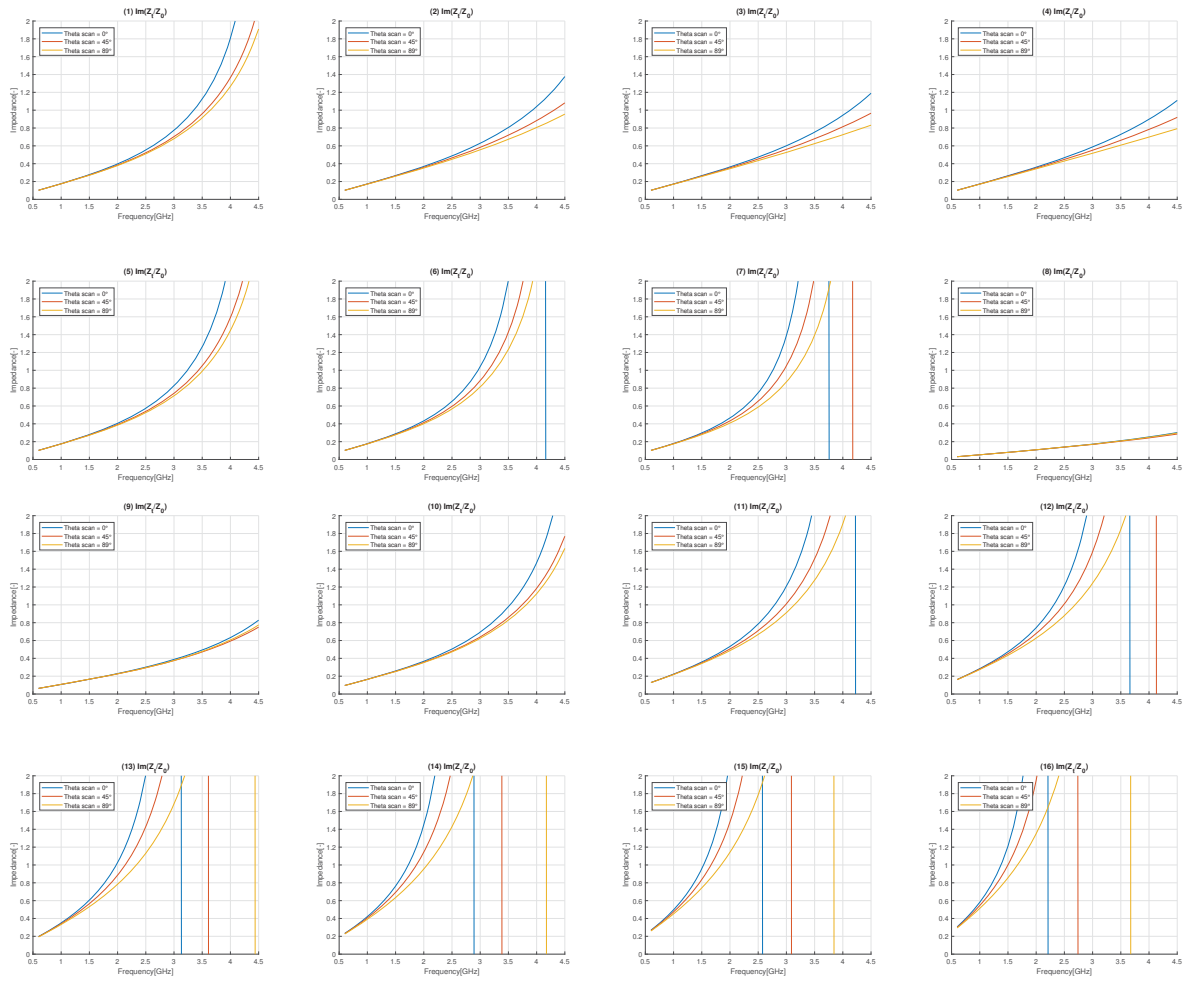
Figure C.5: Z_t iterations, T unit cell (y-axis)

.
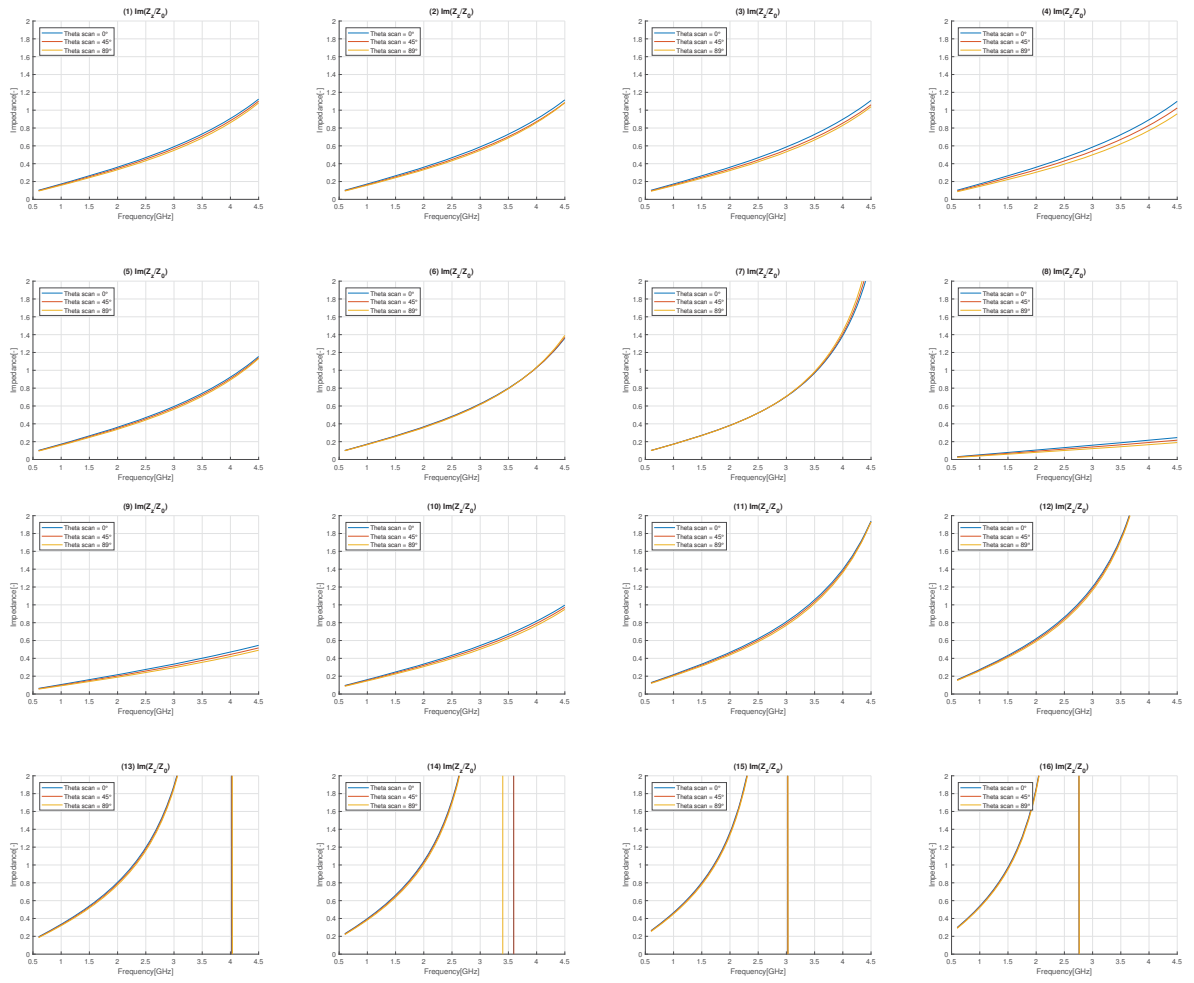
Figure C.6: Z_z iterations, T unit cell (y-axis)

.
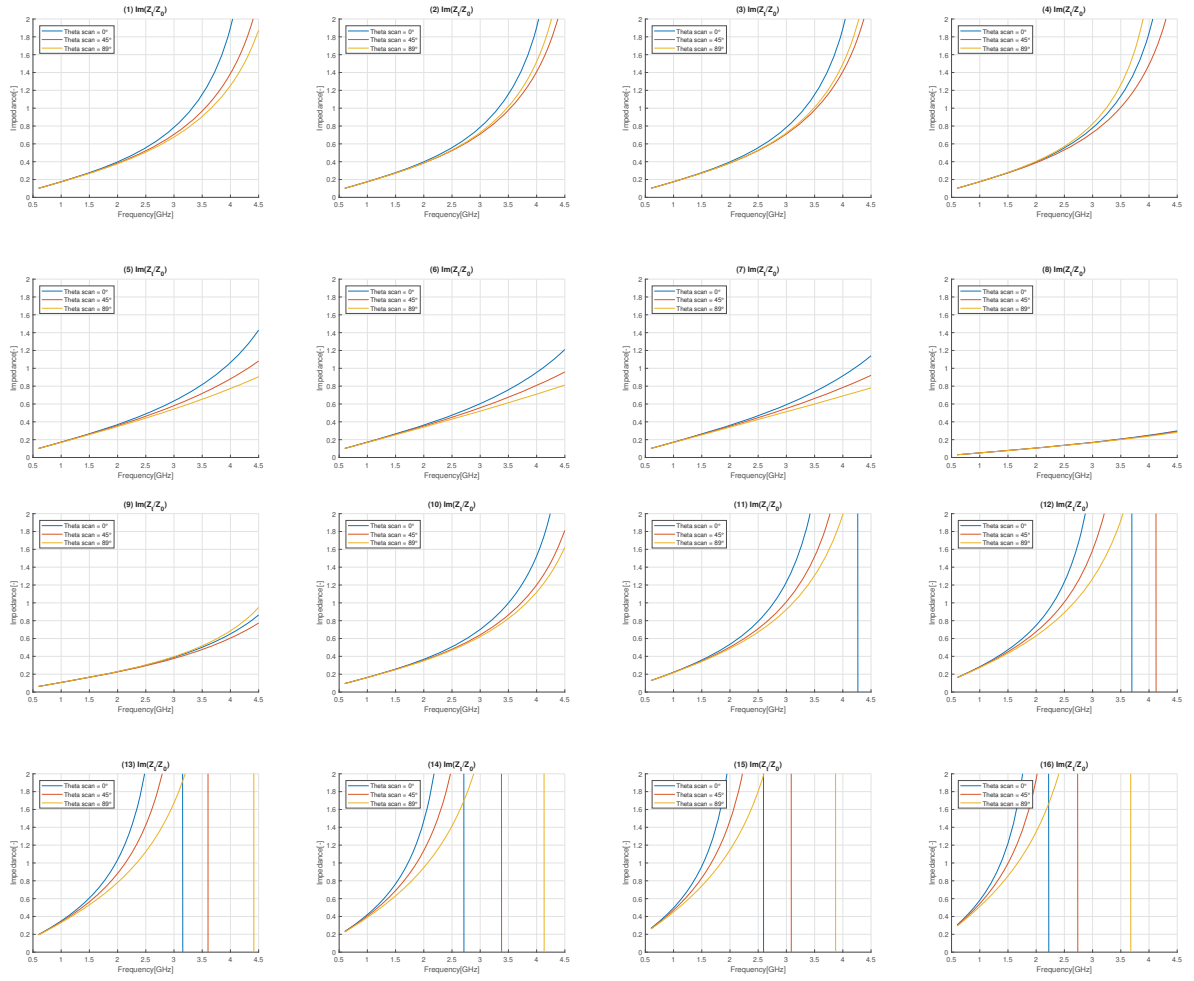
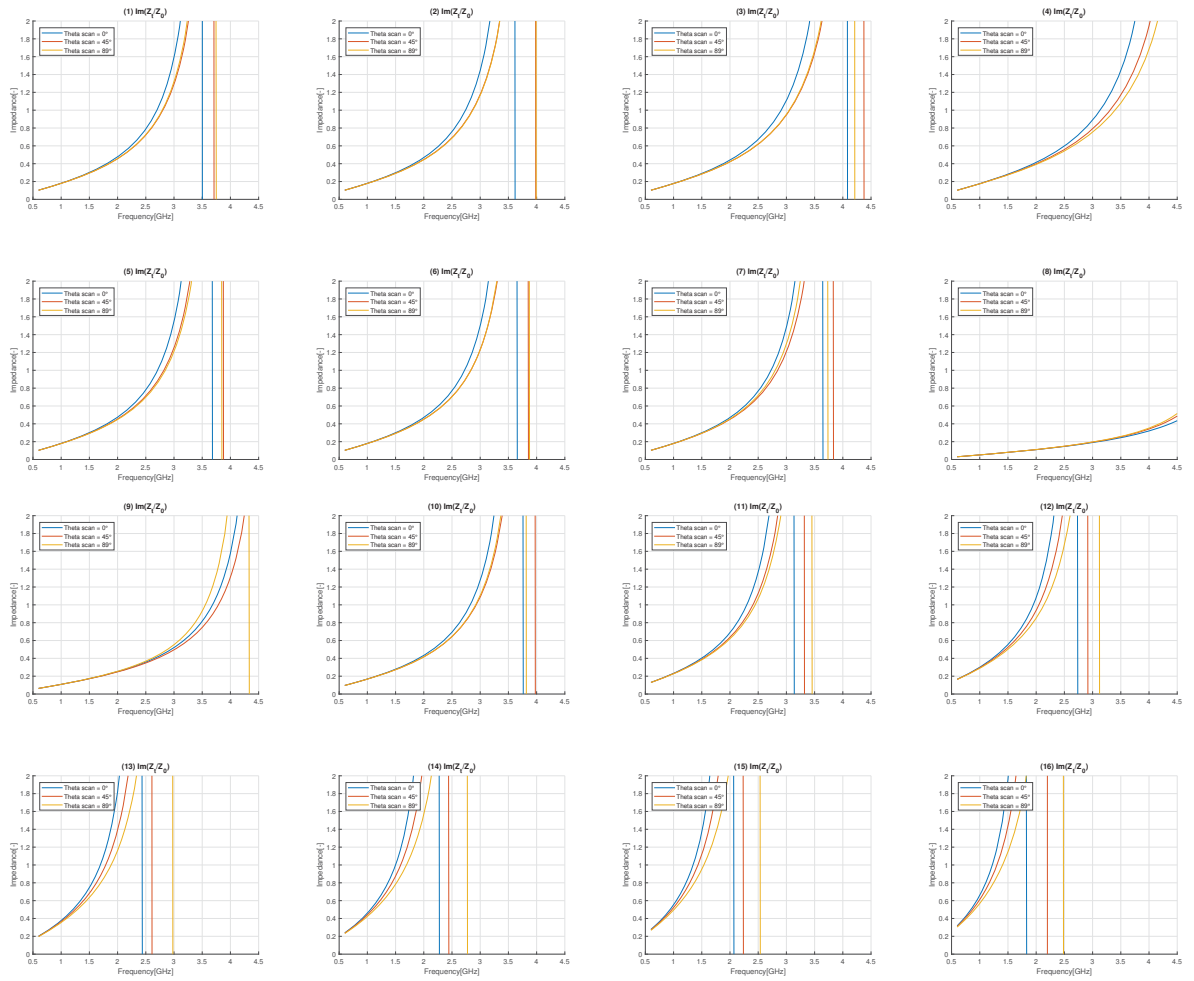Figure C.7: Z_t iterations, X unit cell

.

Figure C.8: Z_Z iterations, X unit cell
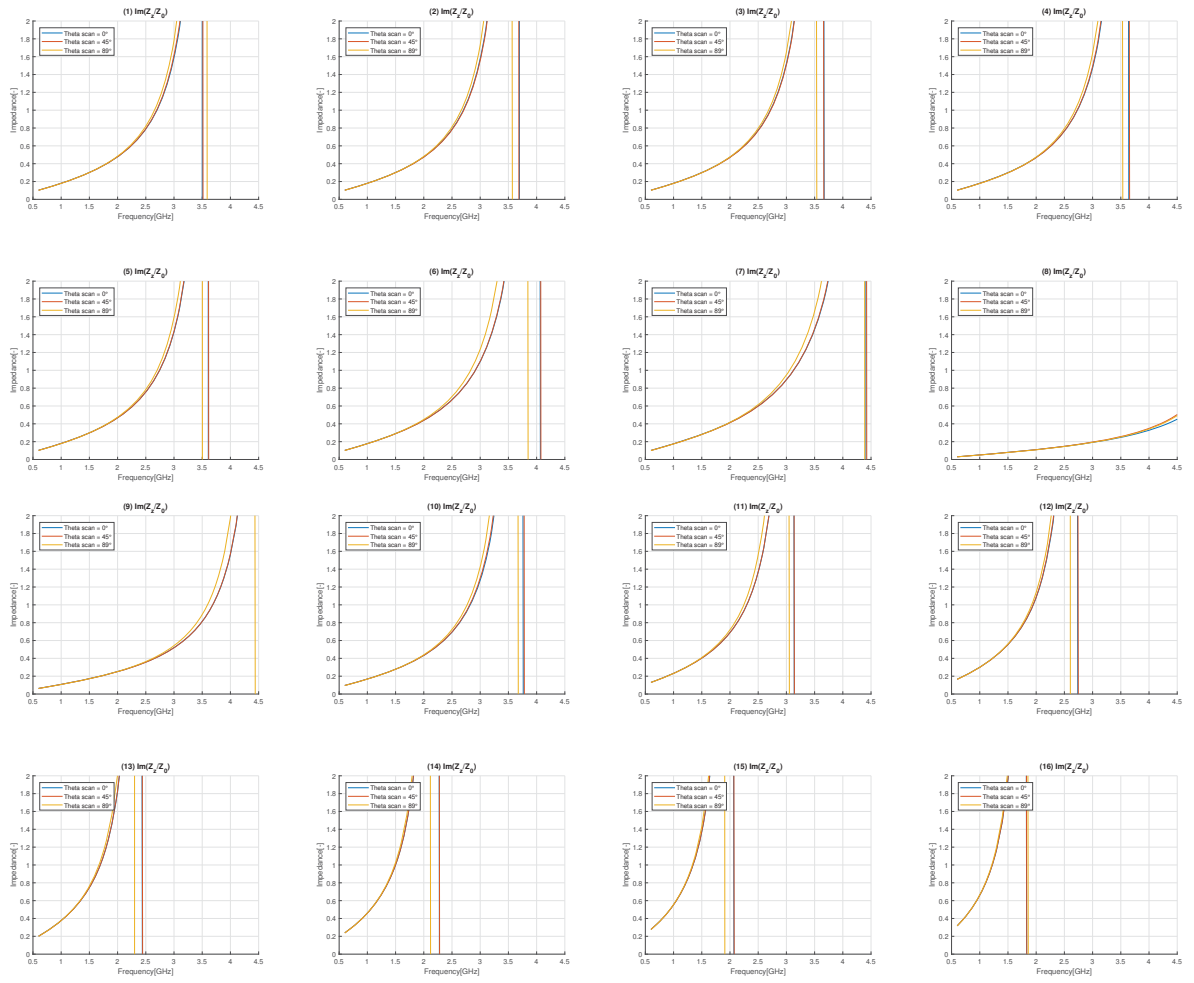
.

Figure C.9: Z_t iterations, Jerusalem cross unit cell

.

Figure C.10: Z_z iterations, Jerusalem cross unit cell

.